NeuroImage 268 (2023) 119860

Contents lists available at ScienceDirect

NeuroImage

journal homepage: www.elsevier.com/locate/neuroimage

High-resolution magnetization-transfer imaging of *post-mortem* marmoset brain: Comparisons with relaxometry and histology

Henrik Marschner[a], André Pampel[a], Roland Müller[a], Katja Reimann[b], Nicolas Bock[c], Markus Morawski[b], Stefan Geyer[a], Harald E. Möller[a,*]

[a] *Max Planck Institute for Human Cognitive and Brain Sciences, Stephanstraße 1a, 04103 Leipzig, Germany*
[b] *Leipzig University, Paul Flechsig Institute of Brain Research, Liebigstraße 19, 04103 Leipzig, Germany*
[c] *McMaster University, Department of Psychology, Neuroscience & Behaviour, 1280 Main Street West, Hamilton, ON L8S4K1, Canada*

ARTICLE INFO

Keywords:
Histology
Iron
Longitudinal relaxation
Macromolecular pool
Magnetization transfer
Myelin
T_1
T_2^*
Transverse relaxation

ABSTRACT

Cell membranes and macromolecules or paramagnetic compounds interact with water proton spins, which modulates magnetic resonance imaging (MRI) contrast providing information on tissue composition. For a further investigation, quantitative magnetization transfer (qMT) parameters (at 3T), including the ratio of the macromolecular and water proton pools, $\mathcal{F}$, and the exchange-rate constant as well as the (observed) longitudinal and the effective transverse relaxation rates (at 3T and 7T), R_1^{obs} and R_2^*, respectively, were measured at high spatial resolution (200 μm) in a slice of fixed marmoset brain and compared to histology results obtained with Gallyas' myelin stain and Perls' iron stain. R_1^{obs} and R_2^* were linearly correlated with the iron content for the entire slice, whereas distinct differences were obtained between gray and white matter for correlations of relaxometry and qMT parameters with myelin content. The combined results suggest that the macromolecular pool interacting with water consists of myelin and (less efficient) non-myelin contributions. Despite strong correlation of $\mathcal{F}$ and R_1^{obs}, none of these parameters was uniquely specific to myelination. Due to additional sensitivity to iron stores, R_1^{obs} and R_2^* were more sensitive for depicting microstructural differences between cortical layers than $\mathcal{F}$.

1. Introduction

Quantitative magnetization transfer imaging (qMTI) is a versatile tool to obtain information on cell membranes or other macromolecular compounds (*e.g.*, proteins) via cross relaxation or proton exchange with water molecules (Edzes & Samulski, 1977, Edzes & Samulski, 1978, Sled, 2018, Wolff & Balaban, 1989). Such semisolid components are not directly visible to standard magnetic resonance imaging (MRI) due to their very short transverse relaxation time, T_2. In a typical MT experiment, the semisolid spin pool is saturated by radiofrequency (RF) irradiation of limited bandwidth applied off resonance of the narrow water line. This leads to a transient water-signal change that can be fitted to a set of differential equations, such as the binary spin-bath (BSB) model (Henkelman et al., 1993). Thereby, information is obtained on the semisolid pool and magnetization exchange rates.

The efficiency of the magnetization transfer (MT) depends on the presence and number of binding sites for water on the semisolid components and on the dynamics of the system (Bryant & Korb, 2005). In brain tissue, and especially in white matter (WM), the most important contribution to cross-relaxation results from myelin that envelops the axons (Koenig et al., 1990, Laule et al., 2007, Möller et al., 2019, Sled, 2018). In particular, galactolipids and cholesterol in the myelin membrane have been proposed as sites with efficient coupling to water molecules (Ceckler et al., 1992, Fralix et al., 1991, Koenig, 1991, Kucharczyk et al., 1994). Previous work has also demonstrated correlations between the relative size of the semisolid pool estimated by qMTI in selected regions of interest (ROIs) and histological measures of myelin content (Schmierer et al., 2007).

The goal of the current work was a more comprehensive, voxel-by-voxel comparison of qMTI of fixed brain and histology. To put the results into a broader context, measurements of the longitudinal rate $R_1 = 1/T_1$ and the effective transverse relaxation rate $R_2^* = 1/T_2^*$ were also integrated in the experiments. Recently, there has been growing interest in using the common marmoset (*Callithrix jacchus*), a New World monkey, in neuroimaging research (Bock et al., 2009, Liu et al., 2011, Newman et al., 2009). While it demonstrates typical primate brain functional organization, its small, lissencephalic brain has no complex folding pattern offering excellent conditions for cortical imaging at high spatial resolution. Further, the brain's overall gray-to-white matter ratio is comparable to that of the human brain, making the marmoset an ideal for quantitative studies of myelin in deep brain structures.

* Corresponding author: Max Planck Institute for Human Cognitive and Brain Sciences, Stephanstraße 1a, 04103 Leipzig, Germany.
E-mail address: moeller@cbs.mpg.de (H.E. Möller).

https://doi.org/10.1016/j.neuroimage.2023.119860.
Received 30 August 2022; Received in revised form 28 December 2022; Accepted 3 January 2023
Available online 5 January 2023.

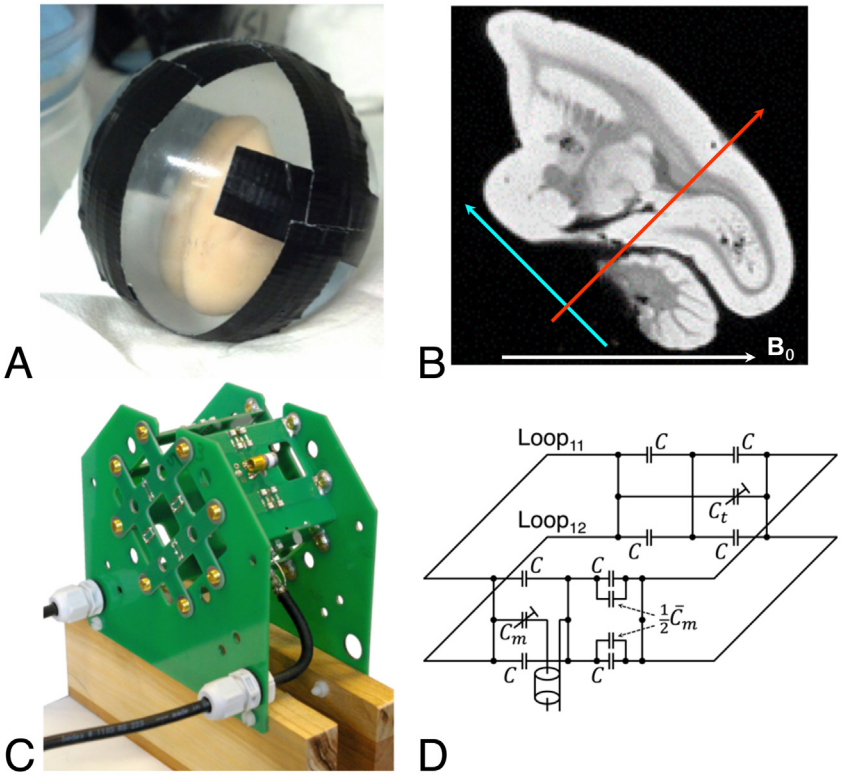

Fig. 1. (A) Fixed marmoset brain inside a spherical acrylic container filled with Fomblin. **(B)** Sagittal slice from an acquisition at 3 T (flip angle, $\alpha = 60°$; repetition time, TR = 300 ms; echo time, TE = 20 ms; 200 µm isotropic nominal resolution). The direction of the main magnetic field, $\mathbf{B}_0$, is from left to right. Arrows indicate approximate positions and orientations of the horizontal zero plane (blue) and the anteroposterior zero plane (red) in the stereotaxic coordinate system of Paxinos et al. (Paxinos et al., 2012). **(C)** Double-Helmholtz transceive RF coil configuration for 3-T MRI with additional venting slots and openings for air circulation. The front part is removable for positioning the spherical sample container. **(D)** Tuning (top) and matching (bottom) circuits of a single Helmholtz pair.

2. Experimental procedures

2.1. Brain specimen

The animal procedures were approved by the NINDS Animal Care and Use Committee. The brain of a male common marmoset (*Callithrix jacchus*) that had died from natural causes at an age of 7.6 years was dissected out and fixed by perfusion with 4% formalin in phosphate-buffered saline (PBS). Subsequently, the specimen was stored in PBS with 0.1% sodium azide (NaN_3) for 17 months before scanning.

For MRI, the brain was centered in an acrylic sphere of 6-cm diameter (Fig. 1A) by gluing the medulla to an alginate socket. The sphere was filled with liquid perfluoropolyether (Fomblin®; Solvay Solexis, Bollate, Italy) to protect the specimen from dehydration and to achieve approximate matching of the magnetic susceptibility at tissue interfaces (Benveniste et al., 1999).

Using the stereotaxic coordinate system defined by Paxinos et al. (Paxinos et al., 2012) as reference (*i.e.*, the horizontal, coronal and sagittal zero planes are defined by the plane passing thorough the lower margin of the orbit and the center of the external auditory meatus, the plane passing through the interaural line, and the plane between both hemispheres, respectively), the brain was oriented inside the magnet such that the magnetic field was approximately parallel to the mid-sagittal plane (*i.e.*, azimuthal angle $\varphi \approx 0°$) at a polar angle $\vartheta \approx 45°$ (Fig. 1B).

2.2. Magnetic resonance image acquisition

All MRI experiments were performed at room temperature (approx. 21 °C) adjusted by the air-conditioning system of the magnet room, but without an additional temperature control unit for the sample. The entire MRI study was split into three parts: *(i)* characterization of the experimental setup and its long-term stability with (gel) phantoms; *(ii)* comprehensive measurements of qMTI parameters and R_1 in the brain specimen at 3 T for subsequent correlation with histology results; and *(iii)* selected measurements of R_1 and R_2^* at 7 T to expand the 3-T results and evaluate their consistency.

2.2.1. Acquisitions at 3 T

A human-scale whole-body scanner (MedSpec 30/100; Bruker Biospin, Ettlingen, Germany) operated under ParaVision 4.0 was used for MRI at 3 T with a custom-built transceiver RF coil. The coil design was made of printed circuit boards (PCBs) and consisted of two perpendicular, quadratic Helmholtz pairs (66 × 66 mm^2; 10 mm-wide, 35 µm-tick copper traces; Fig. 1C) to exploit the lower power requirement (*i.e.*, reduced sample heating during prolonged scanning) of a quadrature coil (Müller et al., 2013b). Eight non-magnetic brass screws on the removable front part (Fig. 1C) provided electrical contact without degrading the homogeneity of the field amplitude, B_0. Inductive coupling between the perpendicular Helmholtz pairs was negligible for equal currents in both loops of one pair. Holes (8 mm diameter) in the PCB at the crossings of the copper traces reduced capacitive coupling caused by mutual capacitances of two pairs (Mispelter et al., 2006). Each loop was pre-tuned to 125 MHz by fixed capacitors (C = 33 pF; 2%, 1111 SMD footprint, 152 CHB series, Temex Ceramics, Pessac, France), connected in series to ensure balanced feeding (Fig. 1D). An additional tuning capacitor C_t (55H01, Johanson, Boonton, NJ) and the feeding coaxial cable were placed exactly halfway between the loops. The feed port was roughly balanced by a matching capacitor C_m of a few pF. Further improvement was achieved by two capacitors of $\bar{C}_m/2$ ($\bar{C}_m$ is the average value of C_m). A PCB with equivalent layout opposite to the feed port carried the tuning circuit. The Helmholtz pairs were connected to a 90° hybrid via 2 m-long coax cables. Lumped resistors of 47 Ω (not related to 50-Ω cable impedance) connected the cable sheaths at 150 mm and 400 mm from the coil to achieve broadband damping of parasitic modes (Boskamp et al., 2012). Bench-top experiments yielded an unloaded Q of 350 and an isolation of the coil pairs by –26 dB. We did not observe relevant detuning, even during scanning sessions of several days.

Experiments in a 50 mm-diameter acrylic sphere filled with agarose gel were performed to measure the RF magnetic transmit field, B_1^+. A

Table 1
Combinations of MT pulse peak amplitudes in angular frequency and magnetic field units, $\omega_{1,max}$ and $B^{+}_{1,max}$, respectively, root-mean-squared MT pulse amplitude, $B^{+}_{1,rms}$, off-resonance frequencies, $\Omega/(2\pi)$, and numbers of averages, N_{av}, used for discrete z-spectrum sampling. Acquisitions indicated by asterisks were excluded from the final analysis due to reduced accuracy (classifier based on fitting the signal in small water pockets to a single-pool model).

$\omega_{1,max}$ [rad/s]	$B^{+}_{1,max}$ [μT]	$B^{+}_{1,rms}$ [μT]	$\Omega/(2\pi)$ [Hz]	N_{av}	$\omega_{1,max}$ [rad/s]	$B^{+}_{1,max}$ [μT]	$B^{+}_{1,rms}$ [μT]	$\Omega/(2\pi)$ [Hz]	N_{av}
1	3.7×10^{-3}	1.8×10^{-3}	50,000	16	3770	14.09	6.88	10,353	6
1100	4.11	2.01	250	16	3770	14.09	6.88	17,624	6
1100	4.11	2.01	426	9	3770	14.09	6.88	30,000	6
1100	4.11	2.01	724	9	4712	17.61	8.60	10,353	6
1100	4.11	2.01	1233	9	*(5341*	*19.96*	*9.75*	*250*	*16)**
1100	4.11	2.01	2099	6	*(5341*	*19.96*	*9.75*	*426*	*9*)*
1100	4.11	2.01	3573	6	5341	19.96	9.75	724	9
1100	4.11	2.01	6082	6	5341	19.96	9.75	1233	9
(2199	*8.22*	*4.01*	*250*	*16)**	5341	19.96	9.75	2099	6
(2199	*8.22*	*4.01*	*426*	*9)**	5341	19.96	9.75	3573	6
(2199	*8.22*	*4.01*	*724*	*9)**	5341	19.96	9.75	6082	6
2199	8.22	4.01	1233	9	5341	19.96	9.75	17,624	6
2199	8.22	4.01	2099	6	5341	19.96	9.75	30,000	6
2199	8.22	4.01	3573	6	7069	26.42	12.90	426	9
2199	8.22	4.01	6082	6	7069	26.42	12.90	724	9
2199	8.22	4.01	10,353	6	7069	26.42	12.90	1233	9
3770	14.09	6.88	250	16	7069	26.42	12.90	2099	6
(3770	*14.09*	*6.88*	*426*	*9)**	7069	26.42	12.90	3573	6
(3770	*14.09*	*6.88*	*724*	*9)**	7069	26.42	12.90	6082	6
3770	14.09	6.88	1233	9	7069	26.42	12.90	10,353	6
3770	14.09	6.88	2099	6	7069	26.42	12.90	17,624	6
3770	14.09	6.88	3573	6	7069	26.42	12.90	30,000	6
3770	14.09	6.88	6082	6					

double-angle method (Hetzer et al., 2009, Insko & Bolinger, 1993) with a three-dimensional (3D) Low-Angle SHot (FLASH) sequence (Haase et al., 1986) was employed with repetition time TR = 5 s, echo time TE = 6.5 ms, flip angles α = 20° and 40°, a field of view (FOV) of 51.2 × 50 × 50 mm^3, and an acquisition matrix 128 × 50 × 50. The estimated distribution of B_1^+ was of sufficient accuracy and homogeneity to allow omitting further corrections of the nominal flip angle (Müller et al., 2013b). Radiofrequency heating experiments (Gaussian pulses; pulse length, τ_p = 10 ms; peak amplitude, $\omega_{1,max}$ = 18,850 rad/s; TR = 30 ms) performed for 1 hour yielded an increase of the core temperature inside the gel phantom by 6 K as compared to 16 K obtained with a single, linearly polarized Helmholtz coil.

The qMTI protocol was adapted from previous *in-vivo* experiments at 3 T in human subjects (Müller et al., 2013a). Magnetization-transfer contrast was generated in a 3D FLASH sequence by applying a preceding 10-ms Gaussian 'MT pulse' in every repetition (*i.e.*, every k-space line). Further acquisition parameters included an 'imaging pulse' flip angle, α = 10°; TR = 32 ms; and TE = 8.2 ms. To obtain so-called 'z-spectra' (Grad & Bryant, 1990), a total of 45 image volumes were recorded with different combinations of eleven logarithmically distributed off-resonance frequencies, $\Omega/(2\pi)$ = 250–50,000 Hz and seven linearly distributed MT pulse amplitudes with $\omega_{1,max}$ = 1–7,069 rad/s (Table 1). The FOV was 38.0 × 27.0 × 25.6 mm^3 with a matrix of 190 × 135 × 128 (*i.e.*, 200 μm isotropic nominal resolution). All measurements were averaged 6–16 times, depending on the expected signal-to-noise ratio (SNR) at the particular off-resonance saturation. The total scan time was 72 hours. Preparatory experiments in agarose gel with an integrated fiberoptic sensor for temperature monitoring showed a stable sample temperature around 23 °C after 3 hours of continuous scanning with this imaging protocol, with residual fluctuations < 0.5 °C depending on the MT pulse amplitude of each specific scan (Supplementary Figure S1). In the measurements of the specimen, the first 3 hours were, therefore, used to achieve stable conditions, and data acquired during this period were not included in the final analysis. The reference gain was re-adjusted after the 3-hour pre-heating period but not during the remaining session. Global B_0 drifts during the experiment were corrected by readjusting the center frequency every 37 to 55 minutes. The total field drift corresponded to roughly 90 Hz (Supplementary Figure S2) during the entire scanning session. Most of this drift was probably due to heating of the gradient coil during the initial 10 hours.

Mapping of the so-called 'observed' longitudinal relaxation rate, $R_1^{obs} = 1/T_1^{obs}$, (Henkelman et al., 1993) at 3 T was performed with the identical image geometry and nominal resolution as for qMTI with a 3D FLASH sequence (TE = 8 ms) and different combinations of α and TR (Fram et al., 1987, Helms et al., 2008) comprising 10°/30 ms, 20°/30 ms, 30°/30 ms, 30°/90 ms, and 30°/200 ms.

Estimates of the spatial distribution of B_0 across the sample were obtained from two-dimensional (2D) multi-echo (ME) gradient-echo acquisitions (α = 60°; TR = 4 s; TE_1 =7.79 ms; 32 echoes with inter-echo time ΔTE = 1.28 ms; 32 slices; 800 μm nominal isotropic resolution) (Chen & Wyrwicz, 1999, Hetzer et al., 2011).

2.2.2. Acquisitions at 7 T

Further measurements of R_1^{obs} and R_2^*, were performed at 7 T on a human-scale whole-body scanner (MAGNETOM 7T; Siemens Healthineers, Erlangen, Germany) operated by *syngo* MR B 17 software. To improve the SNR, a previously described, custom-built miniCP coil was employed, which consisted of two perpendicularly arranged 80-mm circular loops (Weiss et al., 2015). Maps of R_1^{obs} were obtained with the 3D Magnetization-Prepared 2 RApid Gradient Echoes (MP2RAGE) sequence (Marques et al., 2010) and parameters ($\alpha_1 = \alpha_2$ = 8°; TR = 3 s; inversion times, TI_1 = 250 ms, TI_2 = 900 ms; TE = 3.43 ms; matrix 160 × 256 × 112; nominal resolution 176 × 176 × 180 μm; 10 averages) that had been established in former studies of fixed brain tissue (Weiss et al., 2015). Maps of R_2^* were obtained with a 3D ME-FLASH sequence (α = 23°; TR = 42 ms; TE = 6, 14, 22, and 30 ms; matrix 144 × 192 × 120; nominal isotropic resolution 200 μm). Finally, 3D FLASH images (α = 68°; TR = 0.5 s; TE = 35 ms; FOV 25.88 × 36 × 20.8 mm^3; matrix 506 × 704 × 416) were recorded at a high resolution (approx. 50 μm) to improve registration of the magnetic resonance (MR) and histology data by offering sufficiently sharp delineations of tissue boundaries for segmentation and masking purposes.

2.3. Magnetic resonance image processing

2.3.1. Image pre-processing

All 3T images were reconstructed offline using in-house software after export of the raw data. Remaining B_0 drifts leading to subtle shifts (<1 voxel) of the images along phase-encoding direction were corrected by multiplying appropriate phase ramps to the complex-valued k-space data (Jenkinson et al., 2002, Jenkinson & Smith, 2001). Ringing artifacts were reduced by application of a 3D Tukey window with cosine fraction, $r_c = 1/4$. Further filters were not applied.

2.3.2. Magnetization-transfer parameter fitting

In the BSB model, the tissue is subdivided into the free water pool, *'a'*, and the semisolid pool, *'b'*, with equilibrium magnetizations $M_0^{a,b}$ as well as longitudinal and transverse relaxation rates $R_1^{a,b} = 1/T_1^{a,b}$ and $R_2^{a,b} = 1/T_2^{a,b}$, respectively (Edzes & Samulski, 1978, Henkelman et al., 1993, Morrison et al., 1995). The two pools are further assumed to be in close contact allowing exchange of longitudinal magnetizations $M_z^{a,b}$ with pseudo-first-order rate constants $RM_0^{a,b}$ (Henkelman et al., 1993). Under these conditions, the time evolution of the magnetization can be described by simplified Bloch-McConnell equations (McConnell, 1958). Finally, saturation of pool *'b'* caused by the off-resonance irradiation at frequency Ω is modeled by an RF saturation rate (Henkelman et al., 1993):

$$R_{\mathrm{RF}}^b = \pi\omega_1^2 g^b\left(\Omega, T_2^b\right), \tag{1}$$

where ω_1 is the RF field amplitude (in rad/s), and $g^b(\Omega,\ T_2^b)$ is the absorption lineshape function of the semisolid pool. Consistent with previous work (Morrison et al., 1995), we assume that the super-Lorentzian lineshape that arises from partially ordered systems, such as the lipid bilayers of biological membranes (Wennerström, 1973), describes the RF saturation of pool *'b'* sufficiently well in brain tissue. Finally, a scaling factor, σ, is introduced to convert the magnetization computed with the Bloch-McConnell equations into detected signal voltage, $S = \sigma M_z^a$.

Exhaustive details of the procedures for BSB parameter fitting have been published elsewhere (Müller et al., 2013a). Algorithms were implemented in Matlab 9.2.0.538062, R2017a (MathWorks, Natick, MA, USA) using the Global Optimization Toolbox (v3.4.2, R2017a). Unless otherwise stated, least-squares minimization was performed using trust-region-reflective algorithms with parameter boundaries ($10^{-4} \le \sigma M_0^a \le 10^4$; $0 \le M_0^b/M_0^a \le 1$; $6\ \mu\mathrm{s} \le T_1^a \le 10$ s; $6\ \mu\mathrm{s} \le T_2^a \le 10$ s; $6\ \mu\mathrm{s} \le T_2^b \le 20\ \mu\mathrm{s}$; $0 \le RM_0^a \le 1{,}000\ \mathrm{s}^{-1}$). Briefly, fits were based on calculations of the time evolution of the magnetization during the entire pulse sequence using matrix exponentials. The exact timings and shapes of all RF pulses were directly imported from the scanner and used without simplifying assumptions. For better efficiency, polynomial interpolation was employed to calculate the matrix exponentials without bias (Lenich et al., 2019, Müller et al., 2013a). The separately recorded B_0 map was used for voxel-by-voxel correction of all offset frequencies.

Previous work has shown that oscillations may occur in the *z*-spectrum, particularly at small offset frequencies, which result from the nutation of the liquid-pool magnetization and depend on the MT-pulse amplitude (Müller et al., 2013a, Portnoy and Stanisz, 2007). Generally, this effect is difficult to model accurately and may degrade the stability of the fitting procedure. For its further evaluation, the signal amplitude from small pockets of residual water in the alginate socket was fitted to the expected spectrum of a single liquid pool yielding seven data points with residuals outside the 95% confidence interval. Based on this classifier, these seven acquisitions were regarded as potentially affected by oscillations for our experimental conditions and were discarded from the subsequent MT analysis leaving a total of 38 samples in the *z*-spectrum (see Table 1 for details).

In all fits, R_1^b was arbitrarily set to 5 s^{-1} as a fixed parameter (see also below). Previous work has shown that its variation over a meaningful range does not lead to an appreciable effect on *z*-spectra acquired with steady-state off-resonance irradiation (Henkelman et al., 1993, Tyler & Gowland, 2005).

As there is a distinct interdependence of some variables, only five free BSB model parameters can be uniquely determined from fits to the MT data, namely: σM_0^a, $M_0^b/(R_1^a M_0^a)$, RM_0^a, $1/(R_1^a T_2^a)$, and T_2^b (from R_{RF}^b). We note that Henkelman et al. (Henkelman et al., 1993) arbitrarily set $M_0^a = 1$ and, hence, report magnetizations in units of M_0^a. This normalization is, however, not consistently used in the MT literature and is not employed in this work.

2.3.3. Estimation of relaxation rates

To obtain R_1^{obs}, the signal intensities recorded with FLASH and variation of α and TR were separately fitted to (Ernst et al., 1987):

$$S(\alpha, \mathrm{TR}) = S_0 \frac{1 - E_1}{1 - E_1 \cos\alpha} \sin\alpha \text{ with } E_1 \equiv e^{-\mathrm{TR}\cdot R_1^{\mathrm{obs}}} \tag{2}$$

employing a Levenberg-Marquardt algorithm (S_0 is the signal voltage generated by applying a 90° pulse to the fully relaxed spin system). As suggested by Henkelman et al. (1993), knowledge of R_1^{obs} allows computation of R_1^a as an additional BSB model parameter. In particular, a first BSB fit was performed with fixed $T_2^a = 18.5$ ms and free R_1^a with its initial value set to R_1^{obs}. With the obtained results for $\mathcal{F}$ and RM_0^a, a refined R_1^a was computed according to (Henkelman et al., 1993, Müller et al., 2013a):

$$R_1^a = R_1^{\mathrm{obs}} - \frac{\left(R_1^b - R_1^{\mathrm{obs}}\right) RM_0^a \cdot \mathcal{F}}{R_1^b - R_1^{\mathrm{obs}} + RM_0^a}. \tag{3}$$

A final fit with free T_2^a and R_1^a fixed to the above result was then performed to estimate all other free BSB model parameters.

Estimates of R_1^{obs} at 7 T were obtained using the vendor software provided with the MP2RAGE sequence (Marques et al., 2010) without further correction of residual B_1^+ inhomogeneity and those of R_2^* from mono-exponential fits to the TE-dependent signal decay of the ME-FLASH acquisitions.

2.4. Histology procedures

The experiments reported here were embedded in a larger study targeted at cortical parcellation, which defined the choice of the histology procedures. Generally, visualization of myelin is achieved with a variety of staining methods, including Luxol Fast Blue (Klüver & Barrera, 1953) that is often employed in comparisons of MRI and histology results, but also silver staining techniques (Gallyas, 1979, Pistorio et al., 2006), myelin basic protein (MBP) immunohistochemistry (Horton & Hocking, 1997), and many others. Previous work in fixed marmoset brain indicated that Luxol Fast Blue did not achieve a precise border detection due to insufficient resolution (Pistorio et al., 2006). Improved resolution down to the level of individual fibers was obtained with MBP immunohistochemistry and, in particular, with silver staining, which were, therefore, selected for the current work.

The entire formalin-fixed brain was cut in frozen state into 553 coronal sections of 40 µm thickness. During cutting, blockface images (*i.e.*, photographs of the top layer of the cutting block) were taken to support volume reconstruction and co-registration of histological and MR data to a mutual reference frame. Every second section was selected for one out of four different staining procedures, which were applied in an alternating fashion (*i.e.*, the same staining procedure was applied to every eighth section): *(i)* a modified silver impregnation method to reveal myelin, *(ii)* immunohistochemical staining for MBP (anti-MBP, 1:300; Abcam, Cambridge, UK; section immersed in 1% $NaBH_4$ for antigen retrieval), as well as two further antibodies—*(iii)* HuC/HuD antibody (1:500; Life Technologies, Carlsbad, CA, USA) for neurons, and *(iv)* SMI-311 antibody (1:2000; Calbiochem, San Diego, CA, USA) for pan-neurofilaments—that were not used in the current analysis. In an additional session, several odd-numbered sections were stained for ferric iron using Perls' stain. Subsequently, the subscripts 'my', 'MBP' and

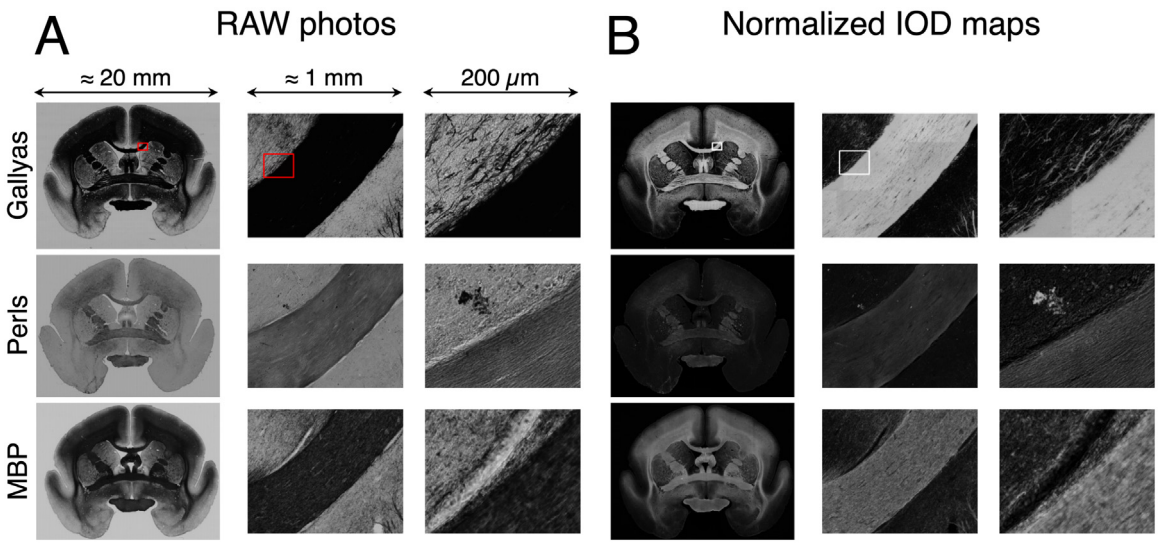

Fig. 2. **(A)** Photographs (raw image format) and **(B)** normalized IOD maps (0.3225 μm in-plane and 55 μm slice resolution) of coronal histology slices at different zoom levels. Rows show, from top (anterior) to bottom (posterior): Gallyas' silver, Perls' stain, and anti-MBP immunohistochemistry. An improvement of contrast in WM achieved by calculating normalized IOD maps is evident on slices stained for myelin (Gallyas' method and anti-MBP immunostaining).

'Fe' are used to indicate histology results obtained with Gallyas', MBP and Perls' stain, respectively.

For a quantitative analysis, initial digitization of multiple slices was performed at relatively low resolution (2.58 μm) on a Zeiss Axio Imager.M1 (Carl Zeiss Microscopy GmbH, Jena, Germany) with an EC Plan-Neofluar 2.5×/0.075 M27 objective and a Zeiss AxioCam HR3 camera. Four sections were then selected (position: approx. 9.75 mm interaural) that showed *(i)* a sufficient variety of anatomical structures and *(ii)* did not indicate major deformations in order to obtain good registration results. Subsequently, maps of the integrated optical density (IOD) were calculated. The sections were digitized monochromatically with 14 bit precision, keeping the brightest areas of the imaged window of the sample holder inside the sensitivity range of the CCD sensor. To reduce influences from potential errors due to inhomogeneous dye distribution, the pixel size was set to 0.3225 μm using an EC Plan-Neofluar 20×/0.50 M27 objective (Floyd, 2013). This permits application of the Beer-Lambert law to calculate the IOD or 'absorbance':

$$A_i = -\log_{10}\frac{I_i}{I_0} \tag{4}$$

from the mean incident intensity, I_0, measured in an empty area of the sample holder, and the transmitted intensity, I_i, at position i. The IOD maps were subsequently normalized to a maximum IOD value of 1 in each slice according to:

$$a_i = \frac{A_i}{\max\left(A_i\right)}. \tag{5}$$

An overview of photographs (at 0.3225 μm) of differently stained slices and corresponding IOD maps is presented in Fig. 2.

2.5. Correlation of MRI and histology data

Image registrations were performed using the Image Processing Toolbox (v9.2) of Matlab. The blockface images were concatenated to yield an uncorrected 3D matrix, and the R_1^{obs} map obtained at 7 T was registered linearly to the blockface reference frame to control for potential misalignment of blockface sections. The low-resolution histological sections were then registered linearly to the appropriate blockface volume sections. The 3-T MR parameter maps were registered non-linearly to the T_1^{obs} map at 7 T to account for inconsistent geometric distortions due to differences in the individual magnetic field profiles of acquisitions from the different scanners.

As linear registration yielded insufficient accuracy for aligning the high-resolution IOD maps with the MR data, the following non-linear procedure was employed: *(i)* The IOD maps were downsampled (factor of 10) to 3.225 μm and manually segmented into different gray matter (GM) and WM regions. Segmentation was performed by drawing masks along tissue boundaries (Supplementary Figure S3) on highly magnified images using GIMP 2.6.12 (http://www.gimp.org). *(ii)* The high-resolution 7-T FLASH images were registered non-linearly to the reference frame while preserving their nominal resolution of 50 μm for sharp tissue boundaries. *(iii)* Slices of the 7-T FLASH dataset at positions matching those of the histology slices were segmented into the same regions as done with the IOD maps. *(iv)* Segment maps of the histology data were non-linearly registered to the corresponding segment maps of the 7-T FLASH data. *(v)* The resulting deformation fields were used to warp the IOD maps, which were subsequently downsampled to 200 μm. The obtained segment maps were also used in separate analyses of the quantitative MR parameters in GM and WM.

Voxel-by-voxel comparisons of co-registered histology and MR data were limited to a single slice shown in Fig. 3A due to concerns of potential variation in the staining intensity between slices (Laule et al., 2006, Pistorio et al., 2006). The GM mask contained contributions from cortical and subcortical structures including anterior cingulate, motor, somatosensory (S1) and insular cortex, as well as caudate, putamen, ventral pallidum, claustrum, amygdaloid (Am) and endopirifom nuclei. The WM mask contained contributions from frontal and temporal WM, the corpus callosum, anterior commissure (ac), internal (ic), external and extreme capsule. The optic chiasm also contained in the WM mask was not included in all analyses but further segmented for additional investigations (see below).

3. Results

3.1. Histology

All stains yielded stable colorations both across the sections and across the entire volume at visual inspection. For WM areas of highest myelination, the digitization revealed a coloration for the Gallyas silver stain that was close to complete opacity for the procedure employed in the current work. These intensely stained areas showed very low transmitted light intensities approaching the sensor's electronic noise level, with corresponding IOD values of $A_{my} < 2$. An example is the optic

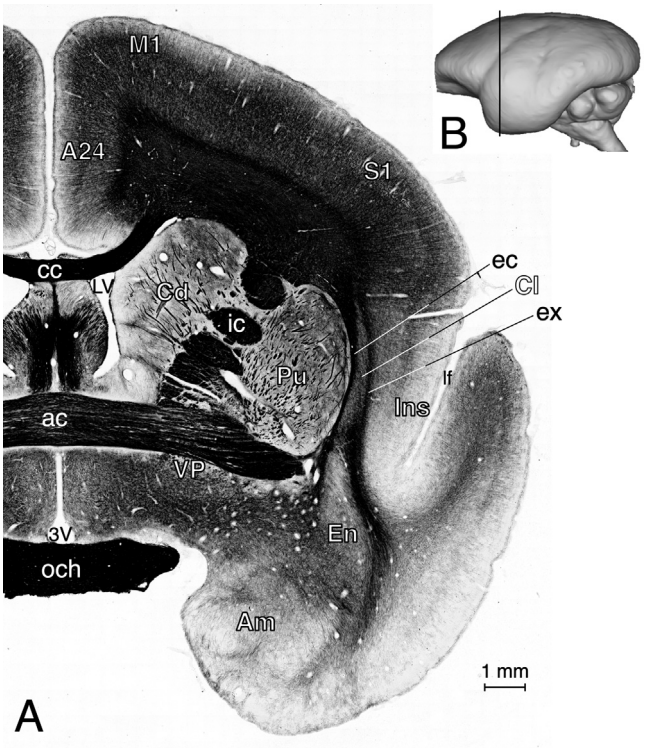

Fig. 3. **(A)** High-resolution section of a coronal slice stained for myelin (Gallyas' silver stain). The slice position is approx. +9.75 mm from the interaural line as marked by a solid line in the stereotaxic view **(B)** [compare, *e.g.*, to Figs. 62a and 62b in (Paxinos et al., 2012) or Coronal Plane: Section 19 in (Yuasa et al., 2010)]. Abbreviations: 3V = 3rd ventricle; A24 = area 24; ac = anterior commissure; Am = amygdaloid nuclei; cc = corpus callosum; Cd = caudate nucleus; Cl = claustrum; ec = external capsule; EN = endopiriform nuclei; ex = extreme capsule; ic = internal capsule; Ins = insula; lf = lateral fissure; LV = lateral ventricle; M1 = primary motor cortex (area 4); och = optic chiasm; Pu = putamen; S1 = primary somatosensory cortex (area 3b); VP = ventral pallidum.

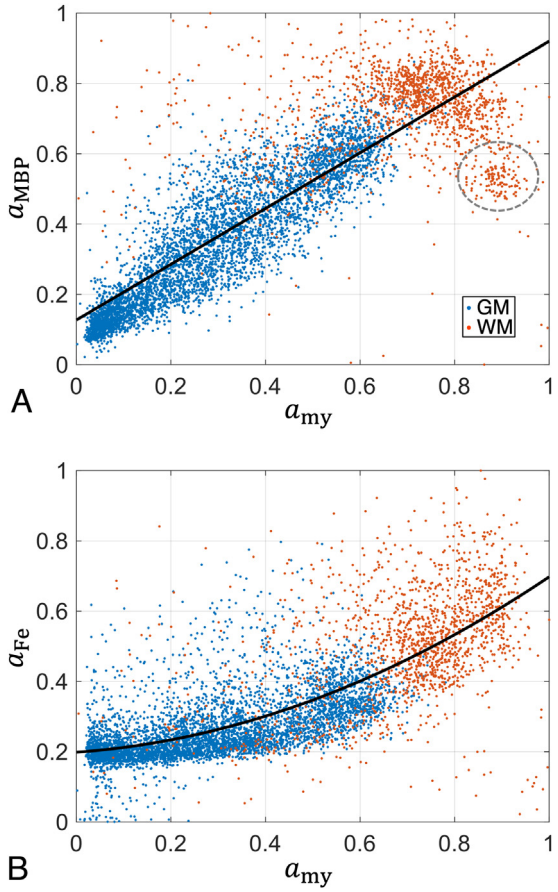

Fig. 4. Scatterplots illustrating histology results (normalized IOD) from two myelin stains and Perls' stain for iron. Blue and red dots indicate voxels in GM ($n = 4{,}964$) and WM ($n = 1{,}538$), respectively. Black solid lines show results from polynomial regression analyses. **(A)** A linear correlation of the two myelin stains, $a_{MBP} = (0.856 \pm 0.012) \cdot a_{my} + (0.0953 \pm 0.0052)$, was obtained for $a_{my} < 0.77$. Deviations from the regression line were evident for voxels in the highly myelinated optic chiasm (data points enclosed by broken line), which were, therefore, eliminated from the analysis. **(B)** The relation between a_{Fe} and a_{my} deviated from a linear behavior if GM and WM voxels (including the optic chiasm) were included in the same analysis, yielding an approximately quadratic empirical relation with $a_{Fe} = (0.404 \pm 0.041) \cdot a_{my}^2 + (0.095 \pm 0.037) \cdot a_{my} + (0.1985 \pm 0.0034)$.

chiasm shown in Fig. 3A. To correct for non-zero intensities caused by electronic noise, the minimal brightness of the slice was defined as "pure back", and all intensity values were shifted accordingly to compute corrected IOD maps.

Voxelwise correlations between the IODs corresponding to different stainings are summarized in Fig. 4. Note that these comparisons have an inherently limited accuracy as the different stains were not obtained from identical but from adjacent sections. While this contributes to the scatter in the correlations, in particular in regions of anatomical boundaries, the effect is assumed to be of minor impact as the histology data were downsampled to the much coarser resolution of the MRI acquisitions (200 µm) in these comparisons.

3.1.1. *Comparison of myelin stains: Gallyas* vs. *MBP*

A comparison of the normalized IOD values of the two myelin stains revealed a positive linear relation between a_{my} and a_{MBP} for values covering approximately three quarters of the normalized range, $0 < a_{my} < 0.77$ (Fig. 4A). Anatomical regions with a_{my} values in this range included GM in addition to WM structures of medium or lower myelination. In WM structures of highest myelination, such as the optic chiasm, a deviation from the regression line was observed, with a_{MBP} values well below those of a_{my}. This inconsistent behavior became particularly evident when GM and WM regions were analyzed separately, yielding a strong positive correlation in GM (Pearson correlation coefficient, $r = 0.894$; error probability $p < 0.001$, Bonferroni-corrected; see Supplementary Table S1), but an insignificant correlation in WM ($r = 0.041$; $p = 0.112$, uncorrected). Due to the apparently more stable coloration across the entire slice obtained with the silver stain, it was selected for the further analyses.

3.1.2. *Comparison of myelin and iron stains*

A comparison of normalized IOD values of iron and myelin stains is presented in Fig. 4B. A similar behavior was found for a_{MBP} (not shown), however, with increased variance compared to a_{my}, consistent with the results in Fig. 4A. Overall, a_{Fe} increased with increasing a_{my}, which could be fitted to an approximately quadratic empirical relation. The observation of a relatively high iron content in WM structures is in line with previous literature demonstrating that oligodendrocytes are the main iron-containing cells in the adult brain (Connor & Menzies, 1996, Möller et al., 2019).

3.2. *Quantitative MRI*

No indications of tissue degradation (*e.g.*, drifting or inconsistent MR parameters) were observed during the experiments at 3 T and, subsequently, at 7 T. The MR images showed a number of signal voids distributed over the entire volume, which were probably caused either by blood clots or by trapped air bubbles. The single slice used for correla-

Table 2
Quantitative results [mean values plus/minus one standard deviation (SD) within the indicated ROI] from MT parameter fitting as well as measurements of the relaxation times T_1^{obs} (at 3 T and 7 T) and T_2^*. Abbreviations: Am = amygdaloid nuclei; cc: corpus callosum; cr = corona radiata; och, c = optic chiasm, central part; och, l = optic chiasm, lateral part; PaC = parietal cortex; Pu = putamen (see also Fig. 3A).

Region	$\mathcal{F}$ 3 T	RM_0^a [s^{-1}]	T_1^a [ms]	T_2^a [ms]	T_2^b [µs]	T_1^{obs} [ms] 3 T	7 T	T_2^* [ms] 7 T
PaC	0.117±0.008	25.2±2.8	443±13	29.7±0.8	9.63±0.18	376± 8	587±15	46.8±3.8
Am	0.086±0.005	23.5±2.3	566±21	39.3±1.8	8.60±0.17	448±11	832±25	64.7±9.7
Pu	0.094±0.006	27.2±3.0	470±17	34.1±1.2	8.65±0.18	392± 9	637±21	43.7±7.4
cc	0.204±0.026	24.2±2.6	379±36	22.3±2.5	10.20±0.42	319±12	439±22	25.2±3.2
cr	0.238±0.013	25.3±2.5	340±16	18.0±0.6	10.93±0.30	302± 8	440±15	22.8±1.5
och, c	0.338±0.032	24.1±4.2	315±13	16.4±1.3	9.63±0.31	286± 5	395±16	17.9±2.0
och, l	0.310±0.032	24.8±4.2	315±19	16.7±1.6	11.43±0.34	280± 6	395±17	21.7±1.0

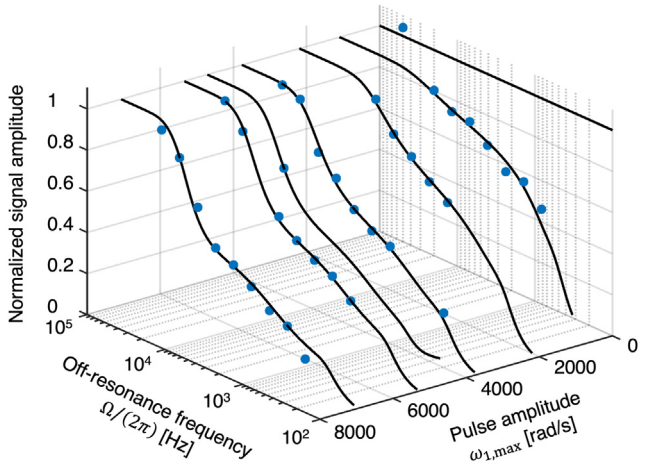

Fig. 5. Experimental *z*-spectrum from a single WM voxel consisting of 38 samples remaining after quality assurance (filled blue circles). The steady-state data were acquired with variation of the MT pulse peak amplitude, $\omega_{1,max}$, and off-resonance frequency, $\Omega/(2\pi)$ (see Table 1). Solid black lines show fitting results based on the BSB model. The data are normalized to the maximum signal intensity obtained by the fit in the displayed range (*i.e.*, the estimated intensity at 50 kHz off resonance).

tions with histology (Fig. 3A) showed a single void located in the left putamen, which was masked out in the quantitative analyses.

Voxelwise fits of the BSB model to the qMT data yielded robust results (Fig. 5), with only small variations of the estimated fitting errors across the entire volume. Examples of various MR parameter maps are shown in Figs. 6A–C. A good differentiation of GM and WM regions was achieved with the pool-size ratio $\mathcal{F} = M_0^b/M_0^a$, whereas the exchange-rate constant RM_0^a showed a limited dynamic range and, hence, largely uniform intensity across the section. Substantial contrast inside the optic chiasm was observed for the transverse relaxation time of the semisolid pool (Fig. 6B), with longer T_2^b in lateral regions as compared to the central part. The contrast obtained with the relaxation parameters R_1^{obs} and R_2^* resembled that of $\mathcal{F}$ with better SNR (Figs. 6D–F). Compared to the 3T result, the R_1^{obs} maps obtained at 7 T had a higher SNR and improved sharpness of tissue boundaries. Averaged values of MT parameters and results from R_1^{obs} and R_2^* mapping inside selected ROIs in cortical GM, subcortical GM and WM are summarized in Table 2.

We note that T_2^a obtained from fits to the BSB model reflects the linewidth of the water signal (modeled as a Lorentzian) and contains additional contributions from inhomogeneous broadening. Therefore, these values are shorter that those measured with a Carr-Purcell-Meiboom-Gill (CPMG) sequence (Henkelman et al., 1993, Müller et al., 2013a, Sled and Pike, 2001), and a quantitative interpretation in terms of tissue composition is not straightforward. An experimental approach that yields additional information on T_2^a in multiple water pools is a combination of the MT preparation with a CPMG readout (Stanisz et al., 1999), which was, however, not integrated in the current work due to time constraints.

Our fixed value of $R_1^b = 5\ s^{-1}$ falls into the range of recent estimates (3.99–6.71 s^{-1} for magnetic fields between 1.5 and 4.7 T) in fresh tissue or under *in vivo* conditions (Helms & Hagberg, 2009, Manning et al., 2021, Wang et al., 2020), whereas earlier MT studies have typically used either $R_1^b = 1\ s^{-1}$ (Levesque and Pike, 2009, Müller et al., 2013a, Sled and Pike, 2001) or $R_1^b = R_1^a$ (Dortch et al., 2011). Although the influence on the *z*-spectrum is expected to be small (Henkelman et al., 1993, Tyler & Gowland, 2005), the choice of a particular R_1^b modulates the results for other fitted BSB parameters. To investigate this influence, we repeated the fits for four randomly selected GM and WM voxels (S1, Am, ac, and ic; see Fig. 3A) with various fixed values for R_1^b. The results are shown in Fig. 7. A change of R_1^b from 1 s^{-1} to 5 s^{-1} produced moderate alterations of $\mathcal{F}$, RM_0^a and R_1^a (19%, –37% and –17%, respectively), whereas only minor effects were obtained for T_2^a and T_2^b (4.7% and 0.5%, respectively). To first order, the variations could be approximated by power laws, $y(R_1^b) = y_0 + \eta(R_1^b)^\kappa$, yielding quadratic deviations from an invariant result (y_0) for $\mathcal{F}$ and T_2^a (κ = 1.93 ± 0.13 and 2.16±0.30, respectively), (sub)linear behavior for R_1^a (κ = 1.089 ± 0.012) and RM_0^a (κ = 0.833 ± 0.016), and κ = 1.50 ± 0.19 for T_2^b (Fig. 7 and Supplementary Table S2). Parameter variations of these orders should be considered in comparisons with literature results, depending on the assumed fixed value. R_1^b is also field and temperature dependent and likely different in fresh and fixed tissue. For example, Wang et al. (2020) observed that R_1^b is reduced by 52% at 7 T compared to 3 T. Using the 3T value for R_1^b in analyses of 7T MT data might, therefore, lead to an overestimation of $\mathcal{F}$ by 9–10% and an underestimation of RM_0^a by 21% considering the results from Fig. 7.

A voxel-by-voxel comparison of R_1^{obs} values at the two field strengths yielded a linear relation for the entire value range (*i.e.*, including all GM and WM voxels), with rates measured at 3 T exceeding those at 7 T by 30–85% (Fig. 8A and Table 2). Plotting R_2^* (Fig. 8B) as a function of R_1^{obs} demonstrated deviations from a common regression line when including all tissue classes. Reasonable linear relations, $R_2^* = (23.06 \pm 0.21) \cdot R_{1,7T}^{obs} - (14.25 \pm 0.32\ s^{-1})$ in GM and $R_2^* = (27.24 \pm 0.42) \cdot R_{1,7T}^{obs} - (18.68 \pm 0.91\ s^{-1})$ in WM, were obtained in separate analyses of the two tissue classes (Figure not shown).

3.3. Correlation of MRI and tissue composition data

The non-linear registration of the multi-modal images enabled a number of explorative univariate analyses on a voxel level, which are summarized in Table 3 and Supplementary Table S1. Strong positive correlations ($p << 0.001$, corrected) with a_{my} were obtained for all proposed MR-derived myelin biomarkers R_1^{obs} ($r \geq 0.571$ at 3 T and $r \geq 0.619$ at 7 T), $\mathcal{F}$ ($r \geq 0.563$) and R_2^* ($r \geq 0.474$) in both GM and WM. Cor-

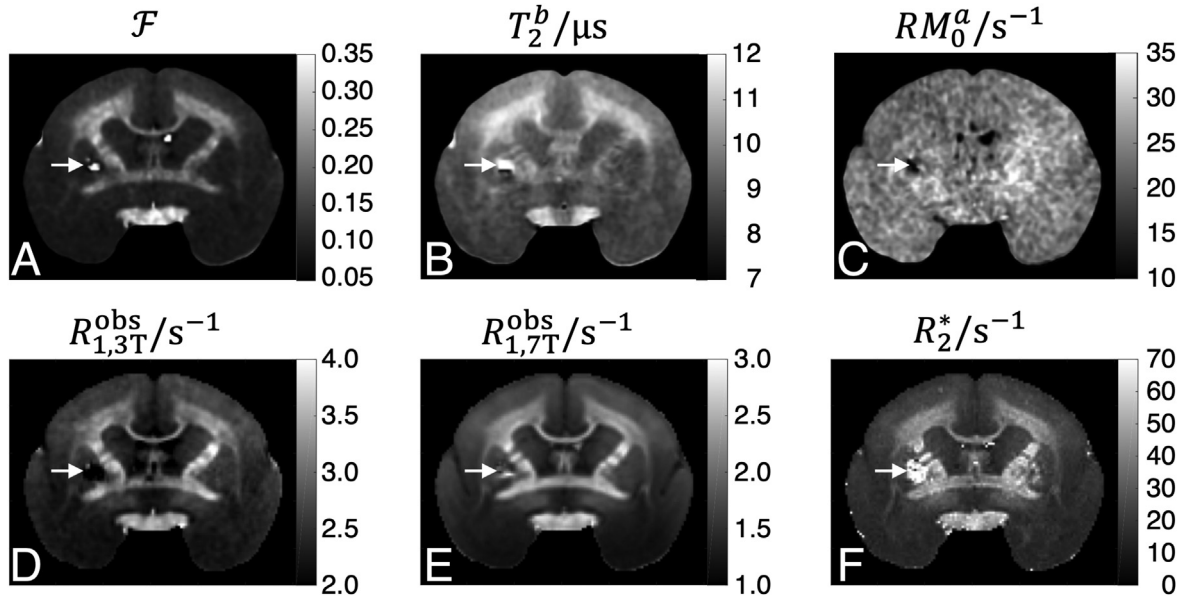

Fig. 6. Maps of MT and relaxation parameters including **(A)** the pool-size ratio $\mathcal{F} = M_0^b/M_0^a$, **(B)** the transverse relaxation time of the semisolid pool T_2^b, and **(C)** the pseudo-first-order rate contract RM_0^a, as well as the observed longitudinal relaxation rate R_1^{obs} measured at **(D)** 3 T and **(E)** 7 T, and **(F)** the effective transverse relaxation rate R_2^* at 7 T. White arrows indicate the position of a signal void in the left putamen, probably due to a blood clot. It is surrounded by a hyperintense area on the R_2^* map because the associated field perturbation reaches out into the adjacent tissue. This region was masked out for the further analysis.

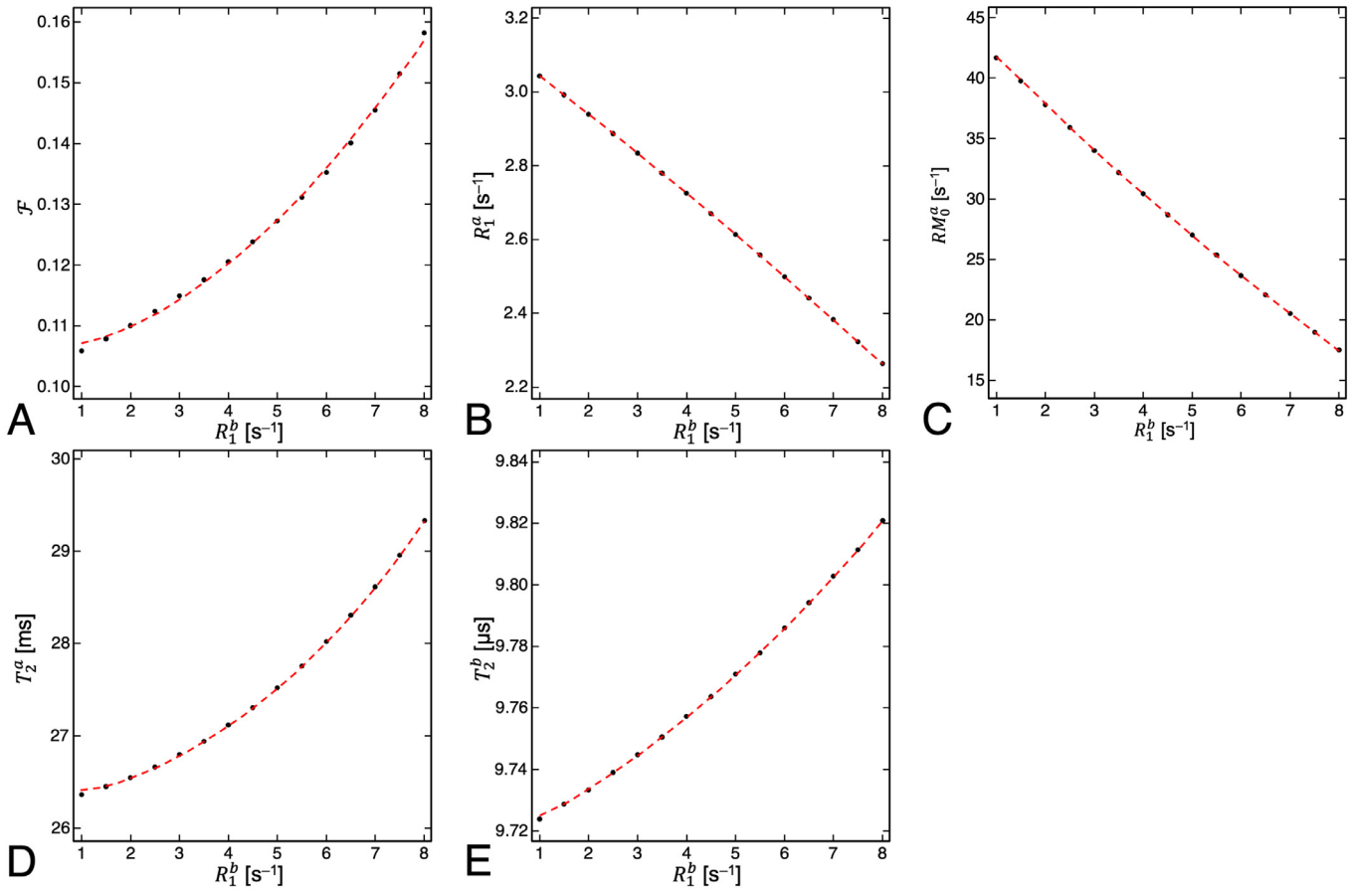

Fig. 7. Impact from the selection of a fixed value for R_1^b on fitted BSB model parameters $\mathcal{F}$ **(A)**, R_1^a **(B)**, RM_0^b **(C)**, T_2^a **(D)** and T_2^b **(E)**. Black filled circles show results from fits of the data in a single voxel in S1 for different R_1^b ranging from 1 s^{-1} and 8 s^{-1}. Red broken lines show empirical fits to a power law, $y(R_1^b) = y_0 + \eta(R_1^b)^\kappa$. Numerical results from the power-law fits are shown in Supplementary Table S2, which also includes further results obtained in other brain regions.

Table 3
Parameter estimates (±SD) from voxelwise univariate linear regressions according to $\boldsymbol{y(x) = c_1 x + c_0}$. Analyses were performed for the whole slice (n = 5,885 voxels) shown in Fig. 3 and, separately, for masks including only GM (n = 4,964 voxels) or only WM (n = 921 voxels). Voxels in the optic chiasm were excluded.

		Whole slice		GM mask		WM mask	
$y(x)$	x	c_1	c_0	c_1	c_0	c_1	c_0
a_{MBP}	a_{my}	0.8555±0.0058	0.1052±0.0025	0.8906±0.0063	0.0887±0.0022	–0.082±0.027	0.816±0.020
$\mathcal{F}$	a_{my}	0.1328±0.0016	0.07108±0.00068	0.0642±0.0013	0.08591±0.00046	0.1303±0.0094	0.1024±0.0070
$\mathcal{F}$	a_{Fe}	0.2248±0.0029	0.05116±0.00096	0.1097±0.0027	0.07578±0.00077	0.1179±0.0098	0.1373±0.0052
RM_0^a/s^{-1}	$\mathcal{F}$	0.1±1.0	23.99±0.13	–33.2±2.0	27.31±0.22	–4.2±3.1	25.78±0.62
RM_0^a/s^{-1}	a_{my}	2.74±0.18	23.013±0.078	2.69±0.23	23.033±0.081	3.89±0.96	22.14±0.71
RM_0^a/s^{-1}	a_{Fe}	8.03±0.30	21.57±0.10	9.38±0.45	21.34±0.13	12.54±0.89	18.63±0.47
$R_{1,3T}^{obs}/s^{-1}$	$\mathcal{F}$	6.626±0.054	1.7337±0.0068	7.107±0.098	1.68±0.011	5.36±0.20	2.001±0.041
$R_{1,3T}^{obs}/s^{-1}$	a_{my}	1.073±0.012	2.1347±0.0051	0.705±0.012	2.2169±0.0043	1.349±0.072	2.079±0.053
$R_{1,3T}^{obs}/s^{-1}$	a_{Fe}	1.957±0.019	1.931±0.0065	1.346±0.025	2.0678±0.0069	1.773±0.063	2.161±0.033
$R_{1,7T}^{obs}/s^{-1}$	$\mathcal{F}$	6.783±0.052	0.7887±0.0065	7.263±0.098	0.730±0.010	4.35±0.17	1.311±0.034
$R_{1,7T}^{obs}/s^{-1}$	a_{my}	1.135±0.011	1.1857±0.0047	0.760±0.012	1.2671±0.0041	1.146±0.058	1.338±0.043
$R_{1,7T}^{obs}/s^{-1}$	a_{Fe}	1.997±0.019	0.9924±0.0063	1.396±0.024	1.1211±0.0069	1.440±0.052	1.441±0.027
R_2^*/s^{-1}	$\mathcal{F}$	189.8±1.9	0.68±0.25	165.9±3.8	2.75±0.40	115.4±6.1	17.7±1.2
R_2^*/s^{-1}	a_{my}	30.67±0.40	12.18±0.17	16.64±0.44	15.23±0.15	31.5±2.0	17.6±1.5
R_2^*/s^{-1}	a_{Fe}	61.36±0.59	4.72±0.19	46.29±0.73	7.85±0.21	41.9±1.8	19.24±0.96

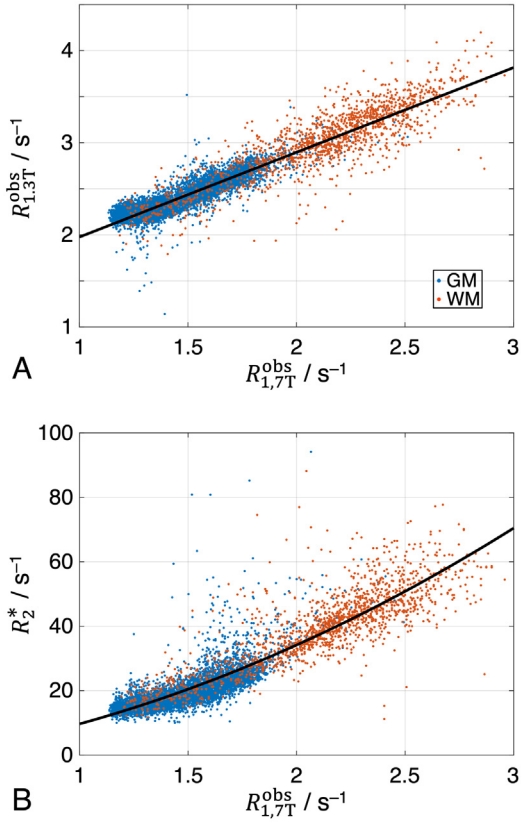

Fig. 8. Scatterplots illustrating voxelwise comparisons of the myelin-sensitive MR parameters R_1^{obs} at 3 T and 7T and R_2^* at 7 T. Blue and red dots indicate voxels in GM (n = 4,964) and WM (n = 921), respectively (same locations as in Fig. 4). Black solid lines show results from regression analyses: **(A)** R_1^{obs} at the two field strengths were linearly correlated for the combined data from GM and WM, $R_{1,3T}^{obs} = (0.9203 \pm 0.0086) \cdot R_{1,7T}^{obs} + (1.056 \pm 0.015\ s^{-1})$. **(B)** The relation between R_2^* and R_1^{obs} (both measured at 7 T) could be fitted to an approximately quadratic empirical relation, $R_2^* = (5.88 \pm 0.78\ s) \cdot (R_{1,7T}^{obs})^2 + (6.8 \pm 2.9) \cdot R_{1,7T}^{obs} - (3.0 \pm 2.5\ s^{-1})$.

relations of RM_0^a were weaker ($r \geq 0.101$) but still highly significant. The correlations with a_{MBP} were similar to those with a_{my} in GM but partly negative or insignificant in WM, which was likely due to inconsistent staining results in regions of highest myelination as mentioned above (see Fig. 4A). Furthermore, all MR parameters correlated with a_{Fe} yielding a similar range of Pearson coefficients as obtained with a_{my}.

Closer inspection of the correlations between the MR parameters R_1^{obs} and R_2^* and a_{my} indicated characteristic deviations from a straight line for the combined data from GM and WM, whereas the dependencies on a_{Fe} were reasonably well described by a common regression line for both segments (Figs. 9A,B and 10A,B). Consistent with previous findings (Stüber et al., 2014), improved descriptions (F-tests; $p < 0.001$, corrected) were obtained with bivariate linear regressions in most cases, according to:

$$y(a_{my}, a_{Fe}) = c_1^{my} a_{my} + c_1^{Fe} a_{Fe} + c_0 \text{ with } y \in \{R_1^{obs}, R_2^*, \mathcal{F}, RM_0^a\}. \quad (6)$$

Table 4 summarizes the fitted linear coefficients c_1^{my}, c_1^{Fe} and c_0. Apart from a scaling of the longitudinal relaxation rate reflecting field dependence (see Fig. 8A), identical behavior was observed for $R_{1,3T}^{obs}$ and $R_{1,7T}^{obs}$.

As the simple BSB model does not differentiate between multiple water environments or between multiple macromolecular compartments, a four-pool model was previously proposed for a more comprehensive characterization of brain tissue, and in particular, WM (Barta et al., 2015, Bjarnason et al., 2005, Levesque & Pike, 2009, Möller et al., 2019, Stanisz et al., 1999). It suggests that $\mathcal{F}$ depends—to first approximation—on contributions from (non-aqueous) myelin and non-myelin dry matter, $M_0^b = M_0^m + M_0^{nm}$, and from myelin water and intra-/extracellular water, $M_0^a = M_0^{mw} + M_0^{iew}$. It is further convenient to define corresponding fractions of the total tissue magnetization, $f^m = M_0^m/(M_0^a + M_0^b)$, $f^{nm} = M_0^{nm}/(M_0^a + M_0^b)$ and $f^a = M_0^a/(M_0^a + M_0^b)$, and to express the normalized IOD (Eq. (5)) obtained with the Gallyas stain as $a_{my} = f^m/f_{max}^m$, which yields:

$$\mathcal{F} = \frac{M_0^m + M_0^{nm}}{M_0^{mw} + M_0^{iew}} = \frac{f_{max}^m}{f^a} a_{my} + \frac{f^{nm}}{f^a}. \quad (7)$$

As shown in Appendix A, this leads to an alternative bivariate relation with linear coefficients c_1^a, c_1^{Fe} and c_0',

$$y(\mathcal{F}, a_{Fe}) = c_1^a \mathcal{F} + c_1^{Fe} a_{Fe} + c_0' \text{ with } y \in \{R_1^{obs}, R_2^*\}, \quad (8)$$

in which the myelin-specific variable a_{my} in Eq. (6) is replaced by $\mathcal{F}$ combining multiple macromolecular contributions. Note that Eq. (8) was obtained assuming fast intercompartmental water exchange. However, exchange is not sufficiently frequent on the R_2^* time scale leading to a multiexponential decay (Du et al., 2007), which cannot be extracted from our measurement with only four gradient echoes. In case of R_2^*, Eq. (8) is, hence, only an empirical relation rather than a model result. Corresponding fits for both relaxation rates are presented in Figs. 9C and

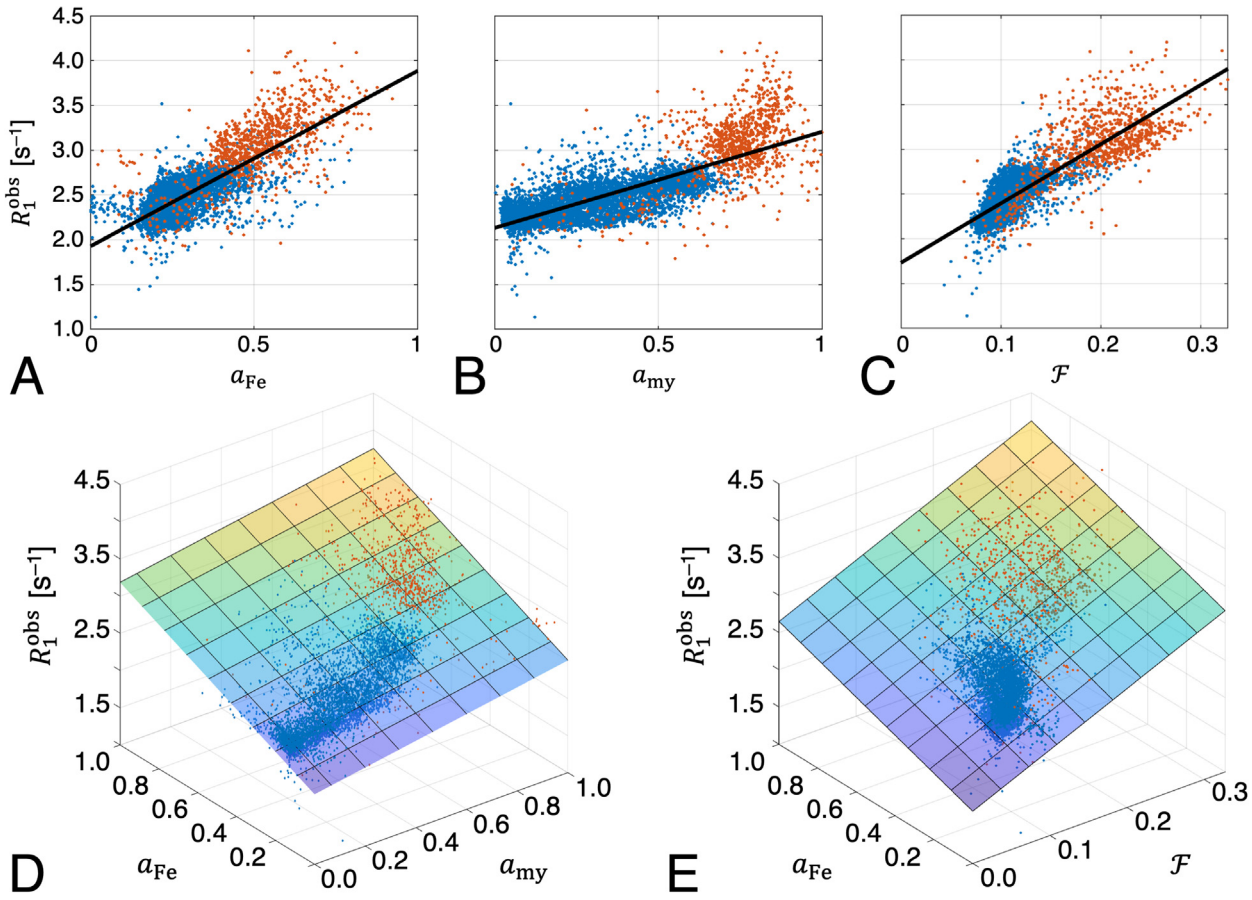

Fig. 9. Scatterplots illustrating voxelwise comparisons of the MR relaxometry parameter $R_{1,3T}^{obs}$ and histology results (normalized IOD) from iron and myelin staining as well as the pool-size ratio $\mathcal{F}$ from the MT experiment. Blue and red dots correspond to voxels in GM and WM, respectively. Consistent results were also obtained with $R_{1,7T}^{obs}$. The top row shows results from univariate regressions of **(A)** $R_{1,3T}^{obs}(a_{Fe})$, **(B)** $R_{1,3T}^{obs}(a_{my})$ and **(C)** $R_{1,3T}^{obs}(\mathcal{F})$. The bottom row shows corresponding bivariate regressions of **(D)** $R_{1,3T}^{obs}(a_{my}, a_{Fe})$ and **(E)** $R_{1,3T}^{obs}(\mathcal{F}, a_{Fe})$ demonstrating significantly improved performance ($p < 0.001$) compared to the univariate fits [$R_{1,3T}^{obs}(a_{my}, a_{Fe})$: $F \geq 1{,}667$; $R_{1,3T}^{obs}(\mathcal{F}, a_{Fe})$: $F \geq 2{,}106$].

10C (results included in Table 4). Compared to results obtained with Eq. (6), the root mean-squared error (RMSE) decreased by 16%, 14% and 9%, and the proportion of the variance explained by the model improved from 71% to 80%, from 76% to 82% and from 69% to 74% for $R_{1,3T}^{obs}$, $R_{1,7T}^{obs}$ and R_2^*, respectively (Supplementary Table S3). This confirms better performance achieved with $\mathcal{F}$ comprising multiple water proton relaxants instead of a_{my}.

A characteristic deviation from a common regression line as observed for the relaxation rates was also evident for the dependency of $\mathcal{F}$ on a_{my} upon including both GM and WM voxels. Surprisingly, we also obtained a similar dependency of $\mathcal{F}$ on a_{Fe} (Fig. 11A). Finally, RM_0^a correlated linearly with both a_{my} and a_{Fe}, though without relevant deviations (within the experimental scatter) from common regression lines for the combined GM and WM data (Figs. 11D,E). Similar to the relaxation rates, improved descriptions of $\mathcal{F}$ were obtained with bivariate linear regression according to Eq. (6) (Fig. 11C), whereas a corresponding improvement was small for RM_0^a (Fig. 11F). In particular, the additional consideration of a_{Fe} in $RM_0^a(a_{my}, a_{Fe})$ yielded very little improvement compared to a univariate relation $RM_0^a(a_{my})$ suggesting that any dependence of RM_0^a on iron content can only be weak.

Comparing the variations of the proposed myelin biomarkers $\mathcal{F}$ and R_1^{obs} with the histology-derived measure a_{my} in GM, a larger (relative) dynamic range is obtained with R_1^{obs} as evidenced by profiles through the primary visual cortex and adjacent WM (Fig. 12). The largest intracortical variability was obtained with R_2^* (Fig. 12D). This is likely due to the greater sensitivity to the presence of iron for R_2^* and R_1^{obs} and a presence of iron and myelin in the same voxel (Callaghan et al., 2015, Draganski et al., 2011, Duyn et al., 2007, Helms et al., 2008).

4. Discussion

4.1. Comparison of the two myelin stains

The mechanism of silver staining of myelin in formalin-fixed brain is assumed to involve reactive foci that bind and reduce silver ions to form metallic clusters, which are visible at microscopy (Larsen et al., 2003, Uchihara, 2007). Such foci are ubiquitously present in the myelin sheath. Similarly, MBP is evenly distributed throughout compact myelin (Brunner et al., 1989). Hence, both histology methods should report on myelin content. Nevertheless, discrepancies in myelin staining patterns obtained with Gallyas' method and with anti-MBP immunostaining (or other techniques) have also been observed previously. This includes both GM [*e.g.*, (Horton & Hocking, 1997)] and WM [*e.g.*, (Kozlowski et al., 2008)] as well as a reduced power of resolving fibers in myelin-dense areas with MBP staining in comparison to Gallyas' method (Pistorio et al., 2006). We note that MBP is located in the myelin main period and that low-molecular mass dyes (*e.g.*, antibodies to the MBP antigen) do not penetrate the membranes in compact myelin but have to diffuse circumferentially to reach the central laminae of the sheath (Georgi et al., 2019, Labadie et al., 2014). Therefore, we speculate that an apparently reduced IOD observed with anti-MBP immunostaining in WM regions of known high myelination might reflect diffusion-limited

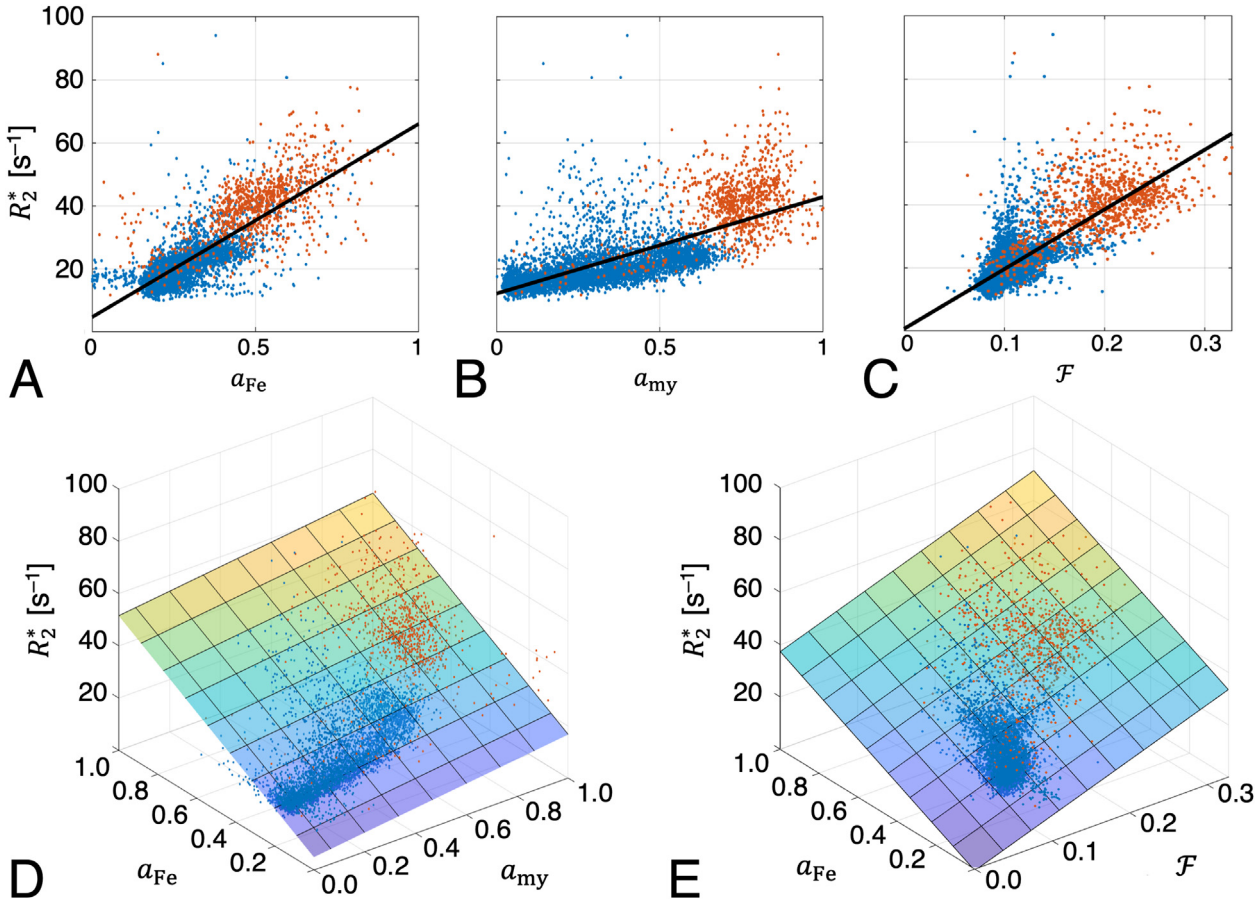

Fig. 10. Scatterplots illustrating voxelwise comparisons of the MR relaxometry parameter R_2^* and histology results (normalized IOD) from iron and myelin staining as well as the pool-size ratio $\mathcal{F}$ from the MT experiment. Blue and red dots correspond to voxels in GM and WM, respectively. The top row shows results from univariate regressions of **(A)** $R_2^*(a_{Fe})$, **(B)** $R_2^*(a_{my})$ and **(C)** $R_2^*(\mathcal{F})$. The bottom row shows corresponding bivariate regressions of **(D)** $R_2^*(a_{my}, a_{Fe})$ and **(E)** $R_2^*(\mathcal{F}, a_{Fe})$ demonstrating significantly improved performance ($p < 0.001$) compared to the univariate fits [$R_2^*(a_{my}, a_{Fe})$: $F \geq 688$; $R_2^*(\mathcal{F}, a_{Fe})$: $F \geq 2{,}108$].

access of the antibodies with less efficient staining of central laminae during the staining procedure due to later arrival times.

4.2. MR Parameters as biomarkers of macromolecules and iron

Our results obtained from a large brain section replicate earlier findings in small tissue specimens, namely bivariate relations between the relaxation rates R_1^{obs} and R_2^* and measures of myelin and iron content (Stüber et al., 2014). However, only the dependencies on a_{Fe} could be approximated by a common regression line for GM and WM, whereas differences between both tissue segments were evident for the dependencies on a_{my}. This suggests *(i)* that a_{Fe} captures contributions from paramagnetic relaxation enhancement reasonably well and *(ii)* that a restriction to only myelin and iron does not achieve a sufficient explanation of the relaxation effects, hinting at contributions from additional relaxants. Improved fits obtained after replacing a_{my} by $\mathcal{F}$ corroborate the hypothesis that R_1^{obs} is not uniquely specific to myelination (and iron) but also impacted by other macromolecular factors, such as the density of cells and neuropil. As an additional non-myelin dry-matter fraction was particularly considered in the pool-size ratio in this analysis (Eq. (7)), it further suggests that $\mathcal{F}$ obtained by qMTI is also not uniquely specific to myelination. In line with this notion, we estimated values of $\mathcal{F} \geq 0.085$ (Fig. 11B) even for very weakly myelinated areas, such as cortical layer II (Nieuwenhuys, 2012, Palomero-Gallagher & Zilles, 2019, Tomassy et al., 2014), confirming that MT is not limited to myelin but includes further contributions.

A 'nonfreezing' water component in biological tissues, characterized by slow diffusion with decreased activation energy, is typically identified with a phase of 'bound water' (*i.e.*, hydration layers) in models of proton cross-relaxation (Bottomley et al., 1984, Escanyé et al., 1984, Fullerton et al., 1982, Koenig, 1991). Recent diffusion experiments suggest a substantial contribution from the myelin water fraction (MWF) to the bound pool (Dhital et al., 2016). However, myelin water alone failed to account for all of the slowly diffusing component, leaving a portion of 31% in WM that was assigned to water associated with other interfacial structures, which may construct the non-myelin compartment probed in our experiments.

The assumption of a non-myelin macromolecular contribution to $\mathcal{F}$ (and R_1^{obs}) is also in line with earlier observations of different GM/WM ratios derived from different myelin-sensitive MRI techniques: Estimates of the MWF in human GM from multi-exponential T_2-decays were approximately 20% of the values in WM (Laule et al., 2007), and 34% in multi-exponential T_1 analyses (Labadie et al., 2014). Note that exchange effects cannot be neglected in longitudinal relaxation (Barta et al., 2015) and probably contribute to a higher MWF estimate in GM from inversion-recovery data. On the T_2 time scale, the assumption of no water exchange between myelin and intra-/extracellular spaces is reasonable although it may not hold for small, weakly myelinated axons. Therefore, we expect an overall good specificity to the myelin compartment for the MWF. For comparison, previous results for $\mathcal{F}$ in human GM *in vivo* were 53% of WM (Sled et al., 2004) in full agreement with our result of 53% in fixed tissue (parietal cortex *vs.* corpus callosum and corona radiata, Table 2). This exceeds typical ratios obtained with the

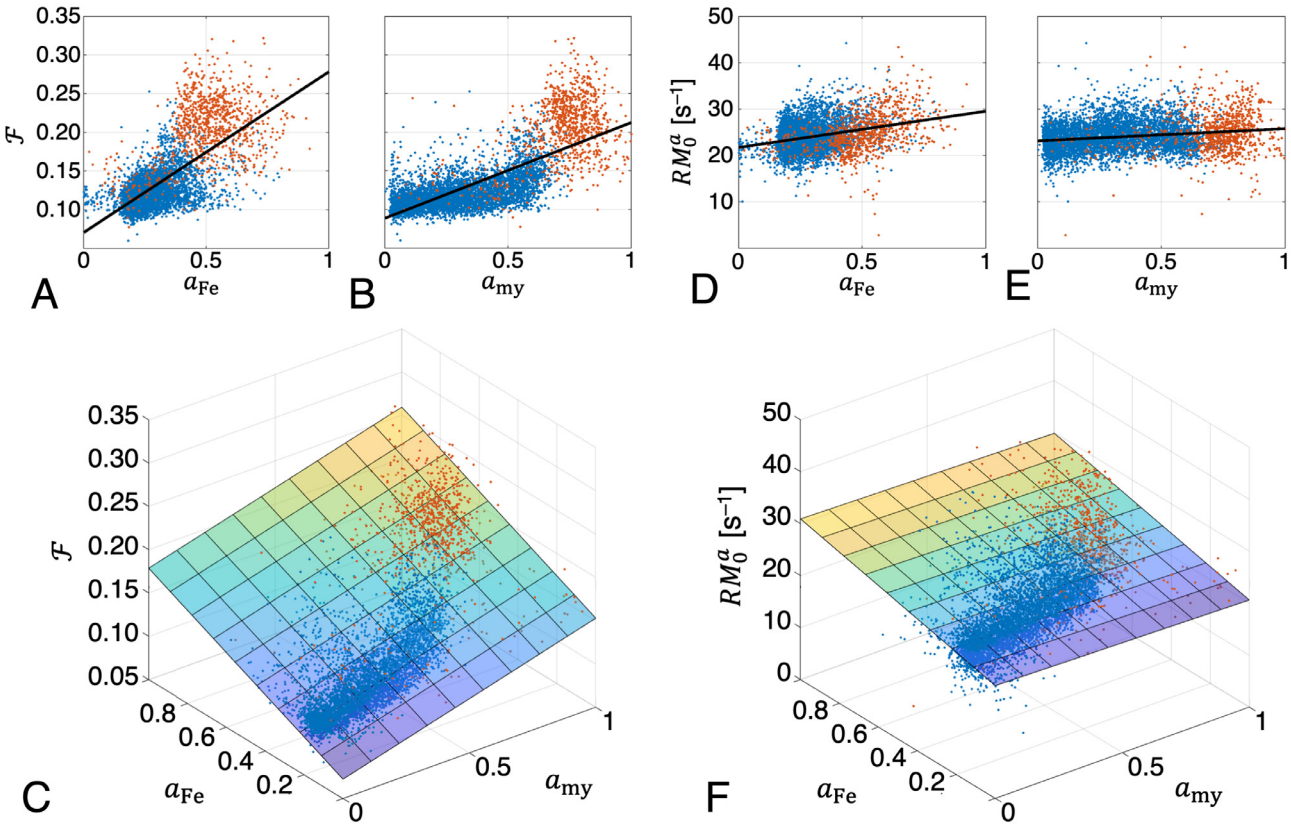

Fig. 11. Scatterplots illustrating voxelwise comparisons of the MT parameters $\mathcal{F}$ **(A–C)** and RM_0^a **(D–F)** and histology results (normalized IOD) from iron and myelin stains. Blue and red dots correspond to voxels in GM and WM, respectively. The top row shows results from univariate regressions of **(A)** $\mathcal{F}(a_{Fe})$ and **(B)** $\mathcal{F}(a_{my})$ as well as **(D)** $RM_0^a(a_{Fe})$ and **(E)** $RM_0^a(a_{my})$. The bottom row shows corresponding bivariate regressions of **(C)** $\mathcal{F}(a_{my}, a_{Fe})$ and **(F)** $RM_0^a(a_{my}, a_{Fe})$. Compared to the univariate fits, performance improved significantly ($p < 0.001$) for $\mathcal{F}(a_{my}, a_{Fe})$ [$F = 1{,}064$ and $1{,}683$ compared to $\mathcal{F}(a_{my})$ and $\mathcal{F}(a_{Fe})$, respectively]. The improvement for $RM_0^a(a_{my}, a_{Fe})$ compared to $RM_0^a(a_{my})$ was less pronounced ($F = 468$, $p < 0.001$) and insignificant when compared to $RM_0^a(a_{Fe})$.

MWF by more than a factor of two. The customary MT ratio, defined as $MTR = 1 - S/S_0$, where S and S_0 are signal amplitudes measured, respectively, with and without application of an MT saturation pulse, even yielded 69% in GM compared to WM in previous work (Vavasour et al., 1998). Besides the 'true' MT contribution, which is extracted by a model fit to compute $\mathcal{F}$, the MTR includes another contribution from direct saturation of the water resonance (Henkelman et al., 2001). This direct effect increases for longer T_1, amplifying the MTR of GM relative to WM. Consequently, the MTR may be a useful qualitative contrast parameter but is rather limited for extracting quantitative information on macromolecular content.

Further consistency checks are obtained from a closer inspection of the fitting results for R_1^{obs} and $\mathcal{F}$:

(i) The ratios of the GM and WM slopes and intercepts from univariate fits of $\mathcal{F}(a_{my})$ to Eq. (7) should be:

$$\mathcal{F}(a_{my}) : \frac{c_{1,GM}}{c_{1,WM}} \approx \frac{f^a_{WM}}{f^a_{GM}} \wedge \frac{c_{0,GM}}{c_{0,WM}} \approx \frac{f^{nm}_{GM} f^a_{WM}}{f^{nm}_{WM} f^a_{GM}}, \tag{9}$$

if $\mathcal{F}$ includes contributions from myelin and non-myelin dry matter with equal weights. If the non-myelin compartment of WM has a similar composition as that of GM (Norton & Cammer, 1984), we would expect $f^{nm}_{GM} \approx f^{nm}_{WM}$. While this is likely an oversimplification, the difference between both fractions is probably small (see Appendix C). The water content is reasonably consistent between mammals and may be estimated from macaque data as $f^a_{GM} \approx 80\%$ and $f^a_{WM} \approx 68\%$ (Faas & Ommaya, 1968, Watanabe et al., 1977). This leads to $f^a_{WM}/f^a_{GM} \approx f^{nm}_{GM} f^a_{WM}/(f^{nm}_{WM} f^a_{GM}) \approx 0.85$, which agrees very well with the observed intercept ratio, $c_{0,GM}/c_{0,WM} = 0.839$ (Table 3). However, the observed slope ratio, $c_{1,GM}/c_{1,WM} = 0.493$, deviates from the prediction, which will be further discussed below.

(ii) A comparison of Eqs. (6) and (8) (see Appendix A) yields $c_1^{my} = c_1^a(f^m_{max}/f^a)$, that is, the ratio of the GM and WM slopes from bivariate fits of $R_1^{obs}(a_{my}, a_{Fe})$ to Eq. (6) should be:

$$R_1^{obs}(a_{my}, a_{Fe}) : \frac{c^{my}_{1,GM}}{c^{my}_{1,WM}} \approx \frac{f^a_{WM}}{f^a_{GM}}. \tag{10}$$

Similar to the result for $\mathcal{F}(a_{my})$, there is a relevant (though smaller) deviation from the predicted value of 0.85: $c^a_{1,GM}/c^a_{1,WM} \approx 0.61$ (average of the 3T and 7T result; Table 4). A potential effect impacting the slopes Eqs. (9) and (10) could be differences in the lipid composition of GM and WM myelin. Galactolipids, which are more abundant in WM than in GM, have been referred to as most 'myelin-typical' lipids (Norton & Cammer, 1984) as their accumulation correlates with the rate of WM myelination during brain maturation (Norton & Poduslo, 1973). They are particularly effective in enhancing water proton relaxation and MT in experiments with model membranes (Kucharczyk et al., 1994). Therefore, a potentially higher percentage of galactolipids in WM myelin might amplify the slope in WM. However, this hypothesis is not supported by our results for the exchange rates, RM_0^a, which could be fitted to a common regression line for GM and WM (Fig. 11B). Alternatively, the deviating slopes might suggest different sensitivities of the MT experiment to the myelin and non-myelin compartments. Remarkably, previous multiparametric characterizations of bovine WM based on a four-pool model yielded a more efficient MT exchange rate for the myelin com-

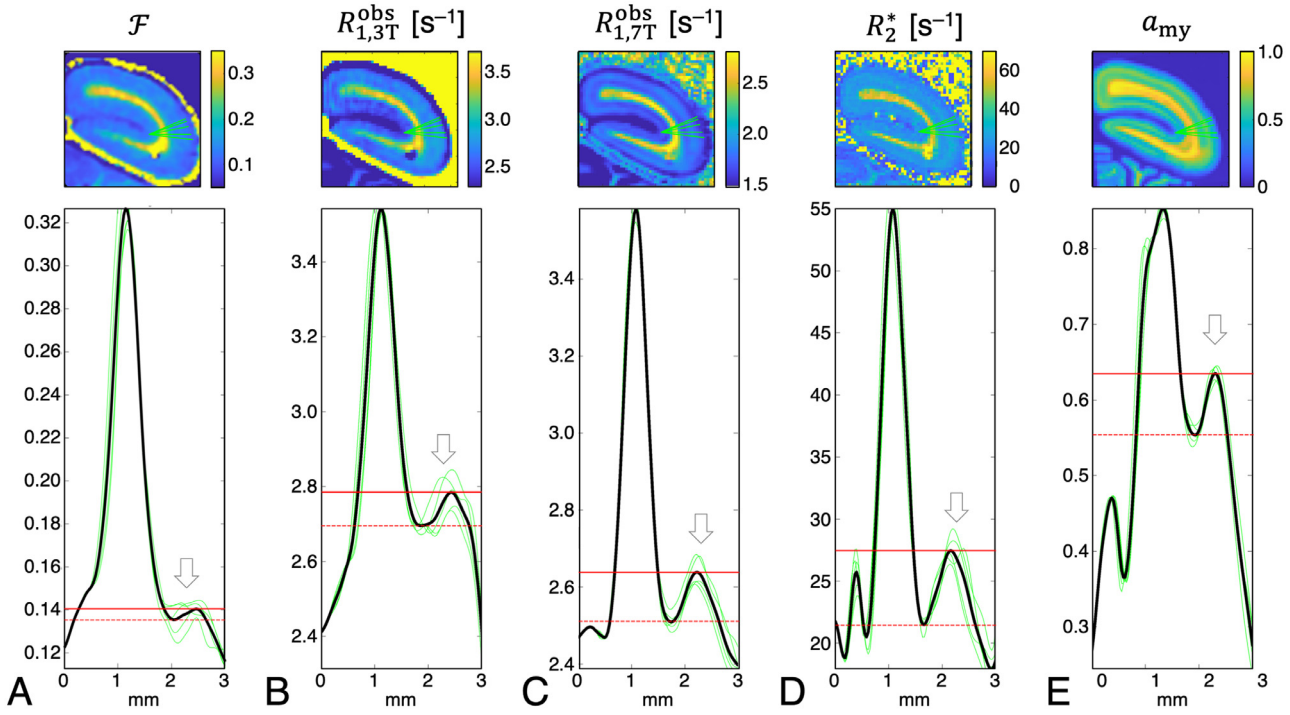

Fig. 12. Parameter maps (top row) from a ROI covering parts of the primary visual cortex (V1) and superpositions of profiles (bottom row; light green lines) of **(A)** $\mathcal{F}$, **(B)** $R_{1,3T}^{obs}$, **(C)** $R_{1,7T}^{obs}$, **(D)** R_2^*, and **(E)** a_{my} through V1 and adjacent WM. Solid black lines represent averages of the individual profiles. Positions corresponding to the profiles are indicated by green lines in the parameter maps. The location of the stria of Gennari on the myelin map is indicated by an arrow. The range of variation of the individual parameters between the local maximum inside the stria of Gennari and the local minimum at the GM/WM border is indicated by solid and broken red lines, respectively. The relative parameter variation along the cortical depth is largest for R_2^*, followed by $R_{1,3T}^{obs}$ and $R_{1,7T}^{obs}$ whereas the smallest range is obtained with $\mathcal{F}$.

partment than for the non-myelin compartment (Bjarnason et al., 2005, Stanisz et al., 1999).

(iii) Fits of $R_1^{obs}(\mathcal{F}, a_{Fe})$ to Eq. (8) should have identical intercepts if further relaxants besides macromolecules and iron are uniformly distributed among tissue classes,

$$R_1^{obs}(\mathcal{F}, a_{Fe}) : \frac{c'_{0,GM}}{c'_{0,WM}} \approx 1, \tag{11}$$

in reasonable agreement with the average experimental results at 3 T and 7 T ($c'_{0,GM}/c'_{0,WM} \approx 0.86 \pm 0.22$; Table 4).

(iv) Expressing R_1^{obs} through BSB model parameters as shown in Appendix B yields the relation $c_1^a \approx (R_1^b - c'_0)RM_0^a/(R_1^b - c'_0 + RM_0^a)$. With $RM_0^a \approx 25.1$ s^{-1} (average over GM and WM), this yields a calculated $c_{1,calc}^a \approx 2.9$ s^{-1} in moderate agreement with the experimental regression result ($c_{1,exp}^a \approx 4.5$ s^{-1}). Some difference between the calculated and the experimental results might be due to a deviation of $R_1^{obs}(\mathcal{F})$ from a strictly linear relation (see Eqs. (A8) and (A9)). However, as this would lead to a slightly reduced $c_{1,exp}^a$ (see Supplementary Figure S4), it does not offer a consistent explanation for the difference between $c_{1,calc}^a$ and $c_{1,exp}^a$. Generally, a larger $c_{1,calc}^a$ would result for a larger R_1^b, indicating that our arbitrarily fixed value of $R_1^b = 5$ s^{-1} might underestimate R_1^b for conditions of our experiments. This underlines the importance of experimental approaches that allow measurement of R_1^b.

Although previous work has shown that the presence of iron affects the MTR (Smith et al., 2009), experiments with the iron storage protein ferritin in model solutions showed that this effect results from water proton T_1 changes rather than an MT effect (Salustri, 1996). Similarly, synthetic iron-loaded melanins decreased the MTR in phantoms without an impact on the estimated macromolecular pool size (Trujillo et al., 2017). *In-vivo* measurements in Parkinson's patients yielded similar trends for MTR and $\mathcal{F}$ in GM, but no significant correlation in the neuromelanin-rich substantia nigra, probably due to a change in T_1 (Trujillo et al., 2017). Taken together, our observed correlations of $\mathcal{F}$ and, to a lesser extent, of RM_0^a with iron content are surprising as the pool sizes should not to be directly influenced by iron stores. At the spatial resolution of our MRI experiments (200 µm), myelin and iron are colocalized in the same voxel (Bizzi et al., 1990, Duyn et al., 2007, Lorio et al., 2014, Morris et al., 1992), which is reflected in our data in the correlation between a_{my} and a_{Fe} (Fig. 4B). Quantitatively, however, this colocalization did not explain the variations of the MT parameters with a_{Fe} well. In this context, a consideration of the different spatial scales of the experiment is important: Both longitudinal relaxation and MT are mediated through dipole-dipole interactions between proton spins and act on a molecular length scale (0.1–1 nm), whereas a cellular scale (1–10 µm) is relevant for the heterogeneous iron distribution (Kiselev & Novikov, 2018). At the cellular level, oligodendrocytes are the most heavily iron-storing cells, followed by microglia, astrocytes and neurons, with approximately three quarters of the total iron being contained in the cytoplasm and mainly localized in lysosomes (Meguro et al., 2008, Reinert et al., 2019). At a subcellular level, iron accumulation was observed in the inner and outer collars of the myelin sheath but not in compact myelin (Meguro et al., 2008). Considering this separation of iron stores and myelin on a micrometer scale, we may assume that histochemical iron measures at the level of an MRI voxel are more associated with membranes of (mostly glial) cell bodies or lysosomes than with myelin. In turn, such a colocalization of iron and a non-myelin macromolecular compartment could produce an apparent correlation

Table 4
Parameter estimates (±SD) from voxelwise bivariate linear regressions according to $y(x_\alpha, x_\beta) = c_1^\alpha x_\alpha + c_1^\beta x_\beta + c_0$. Analyses were performed for the whole slice (n = 5,885 voxels) shown in Fig. 3 and, separately, for masks including only GM (n = 4,964 voxels) or only WM (n = 921 voxels). Voxels in the optic chiasm were excluded.

			Whole slice			GM mask			WM mask		
$y(x_\alpha, x_\beta)$	x_α	x_β	c_1^α	c_1^β	c_0'	c_1^α	c_1^β	c_0'	c_1^α	c_1^β	c_0'
$R_{1,3T}^{obs}/s^{-1}$	a_{my}	a_{Fe}	0.568±0.014	1.244±0.025	1.9407±0.0057	0.467±0.014	0.824±0.027	2.0684±0.0062	0.883±0.058	1.485±0.0590	1.668±0.044
$R_{1,3T}^{obs}/s^{-1}$	$\mathcal{F}$	a_{Fe}	4.486±0.066	0.948±0.021	1.7015±0.0059	5.42±0.10	0.752±0.023	1.6568±0.0095	3.84±0.17	1.321±0.054	1.634±0.035
$R_{1,7T}^{obs}/s^{-1}$	a_{my}	a_{Fe}	0.662±0.013	1.167±0.023	1.0037±0.0053	0.527±0.013	0.806±0.026	1.1218±0.0060	0.773±0.048	1.188±0.048	1.009±0.036
$R_{1,7T}^{obs}/s^{-1}$	$\mathcal{F}$	a_{Fe}	4.619±0.062	0.959±0.019	0.7562±0.0055	5.48±0.10	0.794±0.022	0.7055±0.0094	3.12±0.14	1.072±0.045	1.013±0.029
R_2^a/s^{-1}	a_{my}	a_{Fe}	11.79±0.45	46.57±0.79	4.92±0.18	4.85±0.45	40.86±0.88	7.86±0.20	20.4±1.8	35.2±1.8	7.8±1.3
R_2^a/s^{-1}	$\mathcal{F}$	a_{Fe}	104.2±2.3	37.95±0.72	–0.61±0.20	82.5±3.6	37.24±0.80	1.60±0.34	77.7±5.6	32.7±1.8	8.6±1.2
$\mathcal{F}$	a_{my}	a_{Fe}	0.0848±0.0021	0.1185±0.0036	0.05260±0.00085	0.0481±0.0015	0.0558±0.0030	0.07584±0.00070	0.1040±0.0096	0.0840±0.0098	0.0792±0.0072
RM_0^a/s^{-1}	a_{my}	a_{Fe}	–1.05±0.25	9.35±0.43	21.56±0.10	–0.02±0.28	9.40±0.54	21.34±0.13	–0.06±0.92	12.56±0.94	18.66±0.70

of $\mathcal{F}$ with a_{Fe}. We may further speculate that differently efficient MTs of myelin and non-myelin macromolecules may contribute to the deviations observed for the slope ratios in Eqs. (9) and (10).

The standard BSB model does not consider dipolar relaxation of the semisolid pool because fits of data from fresh WM were relatively insensitive to dipolar order effects in early investigations (Morrison et al., 1995). Recent measurements of the so-called inhomogeneous MT (ihMT) in mouse brain indicate the presence of multiple semisolid pools with different dipolar relaxation times, T_{1D}, with a long-T_{1D} component assigned to myelin and a short-T_{1D} component assigned to non-myelin protons (Duhamel et al., 2019, Hertanu et al., 2021). In particular, they suggest that the long-T_{1D} component may not be appropriately modeled within the standard BSB approach leading to a biased estimate of $\mathcal{F}$ towards short-T_{1D} components and, hence, reduced myelin specificity. This supports the assumption of a contribution from non-myelin macromolecules in our experiments, providing an alternative explanation of the deviating slope ratio from the simplifying prediction according to Eq. (9).

4.3. T_2^b *Contrast in the optic chiasm*

We have recently shown that MT imaging in cerebral WM, and in particular T_2^b, shows an orientation dependence related to the cylindrical symmetry of the myelin membranes enveloping axons (Pampel et al., 2015). Previous work has established that the marmoset chiasm is organized as in other primates and humans (Jeffery et al., 2008): *(i)* Fibers from the lateral optic nerve (*i.e.*, projections from the temporal hemiretina) pass directly (*i.e.*, without approaching the midline) through the lateral chiasm toward the ipsilateral optic tract without a change in fiber order. *(ii)* Fibers from the medial optic nerve (*i.e.*, projections from the nasal hemiretina) cross the midline in the central chiasm toward the contralateral optic tract. Hence, fibers run in approximately anterior-posterior direction in the lateral chiasm but in approximately left-right (and right-left) direction in the central chiasm. Considering the specimen's orientation in the magnet, fibers running through the lateral and central parts were approximately at angles of, respectively, 40° and 90° relative to $\mathbf{B_0}$. The estimated resulting effect size is consistent with the experimental observation and explains the distinct variation of T_2^b in the optic chiasm. According to previous work (Pampel et al., 2015), this orientation effect should not lead to relevant deviations in $\mathcal{F}$ and RM_0^a.

4.4. *Limitations*

A potential confound in qMTI experiments with fresh or fixed tissue *ex vivo* may be due to the temperature dependence of relaxation, in particular, if drifts during the measurement cannot be excluded. Recently, Prevost et al. (2021) investigated the temperature effects in ihMT experiments between 22.5 °C and 37 °C. Remarkably, they observed a relevant impact only in measurements filtered towards a long T_{1D}, whereas unfiltered ihMT was not temperature dependent. The short- and long-term temperature drifts expected for our experimental conditions are <1.5 °C and, hence, much smaller than the temperature range investigated by Prevost et al., supporting the assumption of only a small bias.

Formalin fixation leads to shortened relaxation times and was shown to induce substantial increases (order of 50%) in the pool-size ratio $\mathcal{F}$ (Seifert et al., 2019) or MTR (Schmierer et al., 2008) in MT experiments, which has been attributed to delamination and formation of vacuoles in the myelin sheath. While fixation is required in studies that correlate MRI results and histology, the obtained data cannot be directly transferred to *in vivo* conditions.

5. Conclusions

Voxel-level comparisons of relaxation rates and MT parameters with histochemical myelin and iron stainings in a whole slice of fixed mar-

moset brain at high spatial resolution demonstrate high correlations of $\mathcal{F}$, R_1^{obs}, and R_2^* with each other and with the local myelin and iron content. This finding replicates previous results obtained with either larger ROIs or smaller tissue sections of somewhat reduced variability in the compositions. Correlations with the iron content were relatively well described by the same linear dependence for the entire sample, whereas distinct differences were evident in regressions with the myelin content in GM and WM. The combined results suggest that the macromolecular pool impacting relaxation and MT consists of myelin and non-myelin contributions with a more efficient contribution from the myelin compartment. This might be related to the different lipid composition of the two pools, such as, a higher content of galactolipids in myelin. Despite strong correlations of $\mathcal{F}$ and R_1^{obs} with a_{my} content, neither of the two parameters is uniquely specific to myelination because of non-myelin contributions to both MRI-derived biomarkers. Due to the further impact from iron, R_1^{obs} and R_2^* seem more sensitive for depicting microstructural differences between cortical layers. Given that the macromolecular pool is not exclusively from myelin, bias is expected for qMT-derived myelin surrogates, such as MRI-based g-ratio measurements (Stikov et al., 2015).

Data and code availability statement

Pre-processed MRI and histology raw data and derived MT and relaxometry parameter maps will be made available upon acceptance at https://dataverse.harvard.edu/ (doi: 10.7910/DVN/EQCZJZ). The preprocessing and analyses steps have been well documented in the Methods section. If required, the Matlab scripts used for this purpose can be made available upon request.

Declaration of competing interest

The authors declare no competing interest.

Credit authorship contribution statement

Henrik Marschner: Methodology, Software, Formal analysis, Investigation, Data curation, Writing – review & editing. **André Pampel:** Conceptualization, Methodology, Software, Validation, Investigation, Writing – review & editing. **Roland Müller:** Methodology, Investigation, Writing – review & editing. **Katja Reimann:** Investigation, Data curation, Writing – review & editing. **Nicolas Bock:** Resources, Writing – review & editing. **Markus Morawski:** Conceptualization, Resources, Writing – review & editing. **Stefan Geyer:** Conceptualization, Resources, Writing – review & editing. **Harald E. Möller:** Conceptualization, Methodology, Resources, Writing – original draft, Writing – review & editing, Supervision, Project administration, Funding acquisition.

Data Availability

I have shared a link to my data/code in the manuscript.

Acknowledgements

We thank Afonso Silva for kindly providing the specimen, Marcel Weiss for supporting the 7T acquisitions and Nico Scherf for helpful discussions on analysis strategies. This work was funded (in part) by the Helmholtz Alliance “ICEMED—Imaging and Curing Environmental Metabolic Diseases” (HA-314) through the Initiative and Networking Fund of the Helmholtz Association and by the Max Planck Society.

Supplementary materials

Supplementary material associated with this article can be found, in the online version, at doi:10.1016/j.neuroimage.2023.119860.

Appendix A. Relation between $\mathcal{F}$ and R_1^{obs}

Consistent with previous work, we decompose brain tissue into myelin (m) and non-myelin dry matter (nm) with proton equilibrium magnetizations M_0^m and M_0^{nm}, respectively, as well as water within the myelin sheaths (mw) and in the remaining intra- and extracellular spaces (iew) (Barta et al., 2015, Bjarnason et al., 2005, Levesque & Pike, 2009, Möller et al., 2019, Stanisz et al., 1999). Assuming that intra- and extracellular water are indistinguishable by relaxometry, it is sufficient to consider only two water compartments with proton equilibrium magnetizations M_0^{mw} and M_0^{iew}, leading to the four-pool model expressed by Eq. (7). Note that $\mathcal{F}$ becomes a linear function of a_{my} if f^{nm} is approximately constant. For this case, the slope depends on *(i)* the maximum myelination observed in the *sample*, f^m_{max}, that is, a uniform constant for all GM and WM voxels, and *(ii)* the *voxel's* water content, f^a, which reflects a *specific tissue type*. In the limit of fast water exchange between the myelin and intra-/extracellular compartments, R_1^{obs} can be written as a linear function of the tissue's reciprocal water content (Fullerton et al., 1982):

$$R_1^{obs} = c_1^a \frac{1}{f^a} + c_0^a, \tag{A1}$$

in agreement with experimental results in model systems (Mezer et al., 2013) and *in vivo* (Gelman et al., 2001). However, Eq. (A1) does not consider iron-related relaxation, which may be approximated by a separate linear term. With $f^a = (1+\mathcal{F})^{-1}$, this leads to the empirical relation (Callaghan et al., 2015, Rooney et al., 2007):

$$R_1^{obs} = c_1^a \mathcal{F} + c_1^{Fe} a_{Fe} + c_0', \tag{A2}$$

where $c_0' = c_0^a + c_1^a$. Finally, upon insertion of Eq. (7), we obtain:

$$R_1^{obs} = c_1^a \frac{f^m_{max}}{f^a} a_{my} + c_1^{Fe} a_{Fe} + c_1^a \frac{f^{nm}}{f^a} + c_0'. \tag{A3}$$

A comparison of Eqs. (6) and (A3) yields $c_1^{my} = c_1^a (f^m_{max}/f^a)$ and $c_0 = c_0' + c_1^a (f^{nm}/f^a) = c_0^a + c_1^a [1 + (f^{nm}/f^a)]$. Note that a uniform bivariate relation according to Eq. (6) with identical relaxivities c_1^{my} for GM and WM would only result if the water content does not differ between the tissue classes.

Appendix B. BSB Model-Based Estimation of R_1^{obs}

In the absence of RF irradiation, the Bloch-McConnell equations for the longitudinal magnetization reduce to (McConnell, 1958)

$$\frac{dM_z^{a,b}}{dt} = R_1^{a,b}\left(M_0^{a,b} - M_z^{a,b}\right) - RM_0^{b,a} M_z^{a,b} + RM_0^{a,b} M_z^{b,a} \tag{A4}$$

and can be solved analytically, yielding (Edzes & Samulski, 1977)

$$M_z^a(t) = M_0^a + C_+ e^{-\lambda_+} + C_- e^{-\lambda_-} \tag{A5}$$

with coefficients $C_\pm$ and apparent relaxation rates

$$\lambda_\pm = \frac{1}{2}\left[R_1^a + R_1^b + RM_0^a + RM_0^b \pm \sqrt{\left(R_1^a - R_1^b - RM_0^a + RM_0^b\right)^2 + 4RM_0^a RM_0^b}\right]. \tag{A6}$$

While cross-relaxation between the water and the macromolecular pools is considered in the BSB model, the presence of paramagnetic compounds, such as iron, generates further relaxation pathways for the water protons in tissues, which may be characterized by a linear concentration dependence (see Appendix A) to rewrite R_1^a as (Rooney et al., 2007)

$$R_1^a = R_1^w + c_1^{Fe} a_{Fe}. \tag{A7}$$

R_1^w summarizes contributions from dipolar relaxation of water and all further relaxants, such as dissolved oxygen. With $R_1^{obs} = \lambda_-$

(Henkelman et al., 1993, Müller et al., 2013a) and $RM_0^b = RM_0^a\mathcal{F}$, we obtain:

$$R_1^{\text{obs}} = \frac{1}{2}\left\{ R_1^b + R_1^w + c_1^{\text{Fe}}a_{\text{Fe}} + RM_0^a(1+\mathcal{F}) - \sqrt{\left[R_1^b - R_1^w - c_1^{\text{Fe}}a_{\text{Fe}} + RM_0^a(1-\mathcal{F})\right]^2 + 4\left(RM_0^a\right)^2\mathcal{F}}\right\}, \quad \text{(A8)}$$

which can be approximated, to first order, as

$$R_1^{\text{obs}}\left(\mathcal{F}, a_{\text{Fe}}\right) \approx R_1^w + \frac{\left(R_1^b - R_1^w\right)RM_0^a}{R_1^b - R_1^w + RM_0^a}\cdot\mathcal{F} + c_1^{\text{Fe}}a_{\text{Fe}}. \quad \text{(A9)}$$

Finally, a comparison with Eq. (A2) yields the relations

$$c_1^a \approx \frac{\left(R_1^b - R_1^w\right)RM_0^a}{R_1^b - R_1^w + RM_0^a} \;\wedge\; c_0' \approx R_1^w. \quad \text{(A10)}$$

Further analysis comparing Eqs. (A8) and (A9) shows that a linear dependence of R_1^{obs} on a_{Fe} is an excellent approximation as expected because iron-induced relaxation was introduced an additional linear term. For the range of BSB model parameters observed in our study, deviations from the linear approximation are, however, evident for $\mathcal{F}$, indicating a subtle underestimation of R_1^{obs} in least myelinated GM regions that progressively increased with increasing myelination (see Supplementary Figure S4).

Appendix C. Lipid Pools in GM and WM

According to Norton and Cammer (Norton & Cammer, 1984), fresh human WM contains roughly 300 mg/g dry matter with approximately equal myelin and non-myelin contributions and 700 mg/g water. Of the total water, about 100 mg/g are in the myelin and 600 mg/g in the non-myelin compartment, yielding $\text{MWF}_{\text{WM}} \approx 0.14$. For simplicity, we further assume that cross-relaxation effects, and hence, R_1^{obs} and $\mathcal{F}$, are dominated by (membrane-bound) lipids rather than proteins (Koenig, 1991, Kucharczyk et al., 1994, Pampel et al., 2015). Of the myelin solids, 30% are proteins and 70% or 105 mg/g are lipids, whereas the lipid fraction of the total dry matter is 54.9% or 165 mg/g. This suggests that myelin accounts for 64% of the lipids and non-myelin for the remaining 36% leading to $f_{\text{WM}}^m/f_{\text{WM}}^{nm} \approx 1.8$. Finally, galactolipids are specifically enriched in myelin (Norton and Poduslo, 1973) and particularly efficient cross-relaxation sites (Kucharczyk et al., 1994). They contribute 27.7% of all myelin lipids and 26.4% to the total WM lipid fraction, which corresponds to 29 mg/g and 43 mg/g, respectively. Therefore, 67% of all WM galactolipids are in the myelin and 33% in the non-myelin compartment. Fresh human GM contains about 820 mg/g water and 180 mg/g solids, of which 32.7% or 59 mg/g are lipids. A contribution of 7.3% to the total lipid content is from galactolipids, corresponding to 4.3 mg/g, which defines the maximum possible galactolipid content of GM myelin. An alternative assumption of the same distribution of galactolipids between myelin (67%) and non-myelin (33%) in GM as in WM would lead to approximately 2.9 mg/g. If GM and WM myelin are of similar composition, we expect that 27.5% of all lipids in myelin are galactolipids, and the limiting cases of 2.9–4.3 mg/g computed above yield 10–15 mg/g myelin water and 15–22 mg/g myelin solids (lipids plus proteins), of which 10–16 mg/g are due to myelin lipids. This leads to $\text{MWF}_{\text{GM}} \approx 0.012$–$0.018$ and $f_{\text{GM}}^m/f_{\text{GM}}^{nm} \approx 0.20$–$0.37$. Further comparisons of the estimates for GM and WM yield $\text{MWF}_{\text{GM}}/\text{MWF}_{\text{WM}} \approx 0.09$–$0.13$, $f_{\text{GM}}^m/f_{\text{WM}}^m \approx 0.10$–$0.15$, and $f_{\text{GM}}^{nm}/f_{\text{WM}}^{nm} \approx 0.72$–$0.82$. Given the variation of published values of the lipid composition (Norton & Cammer, 1984, O'Brian & Sampson, 1965), we should consider potential deviations from the above estimates in the order of 10% for the MWF and 25% for the lipid fractions.

References

Barta, R., Kalantari, S., Laule, C., Vavasour, I.M., MacKay, A.L., Michal, C.A., 2015. Modeling T1 and T2 relaxation in bovine white matter. J. Magn. Reson. 259, 56–67. doi:10.1016/j.jmr.2015.08.001.

Benveniste, H., Einstein, G., Kim, K.R., Hulette, C., Johnson, G.A., 1999. Detection of neuritic plaques in Alzheimer's disease by magnetic resonance microscopy. Proc. Natl. Acad. Sci. USA 96, 14079–14084. doi:10.1073/pnas.96.24.14079.

Bizzi, A., Brooks, R.A., Brunetti, A., Hill, J.M., Alger, J.R., Miletich, R.S., Francavilla, T.L., Di Chiro, G., 1990. Role of iron and ferritin in MR imaging of the brain: a study in primates at different field strengths. Radiology 177, 59–65. doi:10.1148/radiology.177.1.2399339.

Bjarnason, T.A., Vavasour, I.M., Chia, C.L.L., MacKay, A.L., 2005. Characterization of the NMR behavior of white matter in bovine brain. Magn. Reson. Med. 54, 1072–1081. doi:10.1002/mrm.20680.

Bock, N.A., Kocharyan, A., Liu, J.V., Silva, A.C., 2009. Visualizing the entire cortical myelination pattern in marmosets with magnetic resonance imaging. J. Neurosci. Methods 185, 15–22. doi:10.1016/j.jneumeth.2009.08.022.

Boskamp, E.B., Fujimoto, M., Amjad, A., Edwards, M., 2012. Broadband damping of cable modes. In: Proceedings of the 20th Annual Meeting of ISMRM, Melbourne, VIC, Australia, p. 2691.

Bottomley, P.A., Foster, T.H., Argersinger, R.E., Pfeifer, L.M., 1984. A review of normal tissue hydrogen NMR relaxation times and relaxation mechanisms from 1–100 MHz: dependence on tissue type, NMR frequency, temperature, species, excision, and age. Med. Phys. 11, 425–448. doi:10.1118/1.595535.

Brunner, C., Lassmann, H., Waehneldt, T.V., Matthieu, J.-M., Linington, C., 1989. Differential ultrastructural localization of myelin basic protein, myelin/oligodendroglial glycoprotein, and 2',3'-cyclic nucleotide 3'-phosphodiesterase in the CNS of adult rats. J. Neurochem. 52, 296–304. doi:10.1111/j.1471-4159.1989.tb10930.x.

Bryant, R.G., Korb, J.-P., 2005. Nuclear magnetic resonance and spin relaxation in biological systems. Magn. Reson. Imaging 23, 167–173. doi:10.1016/j.mri.2004.11.026.

Callaghan, M.F., Helms, G., Lutti, A., Mohammadi, S., Weiskopf, N., 2015. A general linear relaxometry model of R1 using imaging data. Magn. Reson. Med. 73, 1309–1314. doi:10.1002/mrm.25210.

Ceckler, T.L., Wolff, S.D., Yip, V., Simon, S.A., Balaban, R.S., 1992. Dynamic and chemical factors affecting water proton relaxation by macromolecules. J. Magn. Reson. 98, 637–645. doi:10.1016/0022-2364(92)90018-3.

Chen, N.-k., Wyrwicz, A.M., 1999. Correction for EPI distortions using multi-echo gradient-echo imaging. Magn. Reson. Med. 41, 1206–1213. doi:10.1002/(sici)1522-2594(199906)41:6<1206::aid-mrm17>3.0.co;2-l.

Connor, J.R., Menzies, S.L., 1996. Relationship of iron to oligodendrocytes and myelination. Glia 17, 83–93. doi: 10.1002/(SICI)1098-1136(199606)17:2<83::AID-GLIA1>3.0.CO;2-7.

Dhital, B., Labadie, C., Stallmach, F., Möller, H.E., Turner, R., 2016. Temperature dependence of water diffusion pools in brain white matter. NeuroImage 127, 135–143. doi:10.1016/j.neuroimage.2015.11.064.

Dortch, R.D., Li, K., Gochberg, D.F., Welch, E.B., Dula, A.N., Tamhane, A.A., Gore, J.C., Smith, S.A., 2011. Quantitative magnetization transfer imaging in human brain at 3 T via selective inversion recovery. Magn. Reson. Med. 66, 1346–1352. doi:10.1002/mrm.22928.

Draganski, B., Ashburner, J., Hutton, C., Kherif, F., Frackowiak, R.S.J., Helms, G., Weiskopf, N., 2011. Regional specificity of MRI contrast parameter changes in normal ageing revealed by voxel-based quantification (VBQ). NeuroImage 55, 1423–1434. doi:10.1016/j.neuroimage.2011.01.052.

Du, Y.P., Chu, R., Hwang, D., Brown, M.S., Kleinschmidt-DeMasters, B.K., Singel, D., Simon, J.H., 2007. Fast multislice mapping of the myelin water fraction using multicompartment analysis of T2* decay at 3T: a preliminary postmortem study. Magn. Reson. Med. 58, 865–870. doi:10.1002/mrm.21409.

Duhamel, G., Prevost, V.H., Cayre, M., Hertanu, A., Mchinda, S., Carvalho, V.N., Varma, G., Durbec, P., Alsop, D.C., Girard, O.M., 2019. Validating the sensitivity of inhomogeneous magnetization transfer (ihMT) MRI to myelin with fluorescence microscopy. NeuroImage 199, 289–303. doi:10.1016/j.neuroimage.2019.05.061.

Duyn, J.H., van Gelderen, P., Li, T.-Q., de Zwart, J.A., Koretsky, A.P., Fukunaga, M., 2007. High-field MRI of brain cortical substructure based on signal phase. Proc. Natl. Acad. Sci. USA 104, 11796–11801. doi:10.1073/pnas.0610821104.

Edzes, H.T., Samulski, E.T., 1977. Cross relaxation and spin diffusion in the proton NMR of hydrated collagen. Nature 265 (5594), 521–523. doi:10.1038/265521a0.

Edzes, H.T., Samulski, E.T., 1978. The measurement of cross-relaxation effects in the proton NMR spin-lattice relaxation of water in biological systems: hydrated collagen and muscle. J. Magn. Reson. 31, 207–229. doi:10.1016/0022-2364(78)90185-3.

Ernst, R.R., Bodenhausen, G., Wokaun, A., 1987. Principles of Nuclear Magnetic Resonance in One and Two Dimensions. Clarendon Press, Oxford, pp. 124–125.

Escanyé, J.M., Canet, D., Robert, J., 1984. Nuclear magnetic relaxation studies of water in frozen biological tissues. Cross-relaxation effects between protein and bound water protons. J. Magn. Reson. 58, 118–131. doi:10.1016/0022-2364(84)90011-8.

Faas, F.H., Ommaya, A.K., 1968. Brain tissue electrolytes and water content in experimental concussion in the monkey. J. Neurosurg. 28, 137–144. doi:10.3171/jns.1968.28.2.0137.

Floyd, A.D., 2013. Quantitative data from microscopic specimens. In: Suvarna, S.K., Layton, C., Bancroft, J.D. (Eds.), (editors). *Bancroft's Theory and Practice of Histological Techniques*. Churchill Livingstone, London, pp. 40–60.

Fralix, T.A., Ceckler, T.L., Wolff, S.D., Simon, S.A., Balaban, R.S., 1991. Lipid bilayer and water proton magnetization transfer: effect of cholesterol. Magn. Reson. Med. 18, 214–223. doi:10.1002/mrm.1910180122.

Fram, E.K., Herfkens, R.J., Johnson, G.A., Glover, G.H., Karis, J.P., Shimakawa, A., Perkins, T.G., Pelc, N.J., 1987. Rapid calculation of T1 using variable flip angle gradient refocused imaging. Magn. Reson. Imaging 5, 201–208. doi:10.1016/0730-725x(87)90021-x.

Fullerton, G.D., Potter, J.L., Dornbluth, N.C., 1982. NMR relaxation of protons in tissues and other macromolecular water solutions. Magn. Reson. Imaging 1, 209–228. doi:10.1016/0730-725x(82)90172-2.

Gallyas, F., 1979. Silver staining of myelin by means of physical development. Neurol. Res. 1, 203–209. doi:10.1080/01616412.1979.11739553.

Gelman, N., Ewing, J.R., Gorell, J.M., Spickler, E.M., Solomon, E.G., 2001. Interregional variation of longitudinal relaxation rates in human brain at 3.0 T: relation to estimated iron and water contents. Magn. Reson. Med. 45, 71–79. doi:10.1002/1522-2594(200101)45:1<71::aid–mrm1011>3.0.co;2-2.

Georgi, J., Metere, R., Jäger, C., Morawski, M., Möller, H.E., 2019. Influence of the extracellular matrix on water mobility in subcortical gray matter. Magn. Reson. Med. 81, 1265–1279. doi:10.1002/mrm.27459.

Grad, J., Bryant, R.G., 1990. Nuclear magnetic cross-relaxation spectroscopy. J. Magn. Reson. 90, 1–8. doi:10.1002/mrm.1910170216.

Haase, A., Frahm, J., Matthaei, D., Hänicke, W., Merboldt, K.-D., 1986. FLASH imaging. Rapid NMR imaging using low flip-angle pulses. J. Magn. Reson. 67, 258–266. doi:10.1016/j.jmr.2011.09.021.

Helms, G., Dathe, H., Dechent, P., 2008. Quantitative FLASH MRI at 3T using a rational approximation of the Ernst equation. Magn. Reson. Med. 59, 667–672. doi:10.1002/mrm.21542.

Helms, G., Hagberg, G.E., 2009. *In vivo* quantification of the bound pool T1 in human white matter using the binary spin-bath model of progressive magnetization transfer saturation. Phys. Med. Biol. 54, N529–N540. doi:10.1088/0031-9155/54/23/N01.

Henkelman, R.M., Huang, X., Xiang, Q.-S., Stanisz, G.J., Swansosn, S.D., Bronskill, M.J., 1993. Quantitative interpretation of magnetization transfer. Magn. Reson. Med. 29, 759–766. doi:10.1002/mrm.1910290607.

Henkelman, R.M., Stanisz, G.J., Graham, S.J., 2001. Magnetization transfer in MRI: a review. NMR Biomed 14, 57–64. doi:10.1002/nbm.683.

Hertanu, A., Soustelle, L., Buron, J., Le Priellec, J., Cayre, M., Le Troter, A., Varma, G., Alsop, D.C., Durbec, P., Girard, O.M., Duhamel, G., 2021. T_{1D}-weighted ihMT imaging – Part II. Investigating the long- and short-T_{1D} components correlation with myelin content. Comparison with R_1 and the macromolecular proton fraction. Magn. Reson. Med. 87, 2329–2346. doi:10.1002/mrm.29140.

Hetzer, S., Mildner, T., Driesel, W., Weder, M., Möller, H.E., 2009. Shielded dual-loop resonator for arterial spin labeling at the neck. J. Magn. Reson. Imaging 29, 1414–1424. doi:10.1002/jmri.21803.

Hetzer, S., Mildner, T., Möller, H.E., 2011. A modified EPI sequence for high-resolution imaging at ultra-short echo time. Magn. Reson. Med. 65, 165–175. doi:10.1002/mrm.22610.

Horton, J.C., Hocking, D.R., 1997. Myelin patterns in V1 and V2 of normal and monocularly enucleated monkeys. Cereb. Cortex 7, 166–177. doi:10.1093/cercor/7.2.166.

Insko, E.K., Bolinger, L., 1993. Mapping of the radiofrequency field. J. Magn. Reson. A 103, 82–85. doi:10.1006/jmra.1993.1133.

Jeffery, G., Levitt, J.B., Cooper, H.M., 2008. Segregated hemispheric pathways through the optic chiasm distinguish primates from rodents. Neuroscience 157, 637–643. doi:10.1016/j.neuroscience.2008.09.021.

Jenkinson, M., Bannister, P., Brady, M., Smith, S., 2002. Improved optimization for the robust and accurate linear registration and motion correction of brain images. NeuroImage 17, 825–841. doi:10.1016/s1053-8119(02)91132-8.

Jenkinson, M., Smith, S., 2001. A global optimisation method for robust affine registration of brain images. Med. Image Anal. 5, 143–156. doi:10.1016/s1361-8415(01)00036-6.

Kiselev, V.G., Novikov, D.S., 2018. Transverse NMR relaxation in biological tissues. NeuroImage 182, 149–168. doi:10.1016/j.neuroimage.2018.06.002.

Klüver, H., Barrera, E., 1953. A method for the combined staining of cells and fibers in the nervous system. J. Neuropathol. Exp. Neurol. 12, 400–403. doi:10.1097/00005072-195312040-00008.

Koenig, S.H., 1991. Cholesterol of myelin is the determinant of gray-white contrast in MRI of brain. Magn. Reson. Med. 20, 285–291. doi:10.1002/mrm.1910200210.

Koenig, S.H., Brown III, R.D., Spiller, M., Lundbom, N., 1990. Relaxometry of brain: why white matter appears bright in MRI. Magn. Reson. Med. 14, 482–495. doi:10.1002/mrm.1910140306.

Kozlowski, P., Raj, D., Liu, J., Lam, C., Yung, A.C., Tetzlaff, W., 2008. Characterizing white matter damage in rat spinal cord with quantitative MRI and histology. J. Neurotrauma 25, 653–676. doi:10.1089/neu.2007.0462.

Kucharczyk, W., Macdonald, P.M., Stanisz, G.J., Henkelman, R.M., 1994. Relaxivity and magnetization transfer of white matter lipids at MR imaging: importance of cerebrosides and pH. Radiology 192, 521–529. doi:10.1148/radiology.192.2.8029426.

Labadie, C., Lee, J.-H., Rooney, W.D., Jarchow, S., Aubert-Frécon, M., Springer Jr, C.S., Möller, H.E., 2014. Myelin water mapping by spatially regularized longitudinal relaxographic imaging at high magnetic fields. Magn. Reson. Med. 71, 375–387. doi:10.1002/mrm.24670, Erratum. *Magn. Reson. Med.* 2015; 74: 150310.1002/mrm.25974.

Larsen, M., Bjarkam, C.R., Stoltenberg, M., Sørensen, J.C., Danscher, G., 2003. An autometallographic technique for myelin staining in formaldehyde-fixed tissue. Histol. Histopathol. 18, 1125–1130. doi:10.14670/HH-18.1125.

Laule, C., Leung, E., Li, D.K.B., Traboulsee, A.L., Paty, D.W., MacKay, A.L., Moore, G.R.W., 2006. Myelin water imaging in multiple sclerosis: quantitative correlations with histopathology. Mult. Scler. 12, 747–753. doi:10.1177/1352458506070928.

Laule, C., Vavasour, I.M., Kolind, S.H., Li, D.K.B., Traboulsee, T.L., Moore, G.R.W., MacKay, A.L., 2007. Magnetic resonance imaging of myelin. Neurotherapeutics 4, 460–484. doi:10.1016/j.nurt.2007.05.004.

Lenich, T., Pample, A., Mildner, T., Möller, H.E., 2019. A new approach to Z-spectrum acquisition: prospective baseline enhancement (PROBE) for CEST/nuclear Overhauser effect. Magn. Reson. Med. 81, 2315–2329. doi:10.1002/mrm.27555.

Levesque, I.R., Pike, G.B., 2009. Characterizing healthy and diseased white matter using quantitative magnetization transfer and multicomponent T2 relaxometry: a unified view via a four-pool model. Magn. Reson. Med. 62, 1487–1496. doi:10.1002/mrm.22131.

Liu, J.V., Bock, N.A., Silva, A.C., 2011. Rapid high-resolution three-dimensional mapping of T1 and age-dependent variations in the non-human primate brain using magnetization-prepared rapid gradient-echo (MPRAGE) sequence. *NeuroImage* 56: 1154–1163. https://doi.org/10.1016/j.neuroimage.2011.02.075.

Lorio, S., Lutti, A., Kherif, F., Ruef, A., Dukart, J., Chowdhury, R., Frackowiak, R.S., Ashburner, J., Helms, G., Weiskopf, N., Draganski, B., 2014. Disentangling *in vivo* the effects of iron content and atrophy on the ageing human brain. NeuroImage 280–289. doi:10.1016/j.neuroimage.2014.09.044.

Manning, A.P., MacKay, A.L., Michal, C.A., 2021. Understanding aqueous and non-aqueous proton T1 relaxation in brain. J. Magn. Reson. 323, 106909. doi:10.1016/j.jmr.2020.106909.

Marques, J.P., Kober, T., Krueger, G., van der Zwaag, W., Van de Moortele, P.-F., Gruetter, R., 2010. MP2RAGE, a self bias-field corrected sequence for improved segmentation and T1-mapping at high field. NeuroImage 49, 1271–1281. doi:10.1016/j.neuroimage.2009.10.002.

McConnell, H.M., 1958. Reaction rates by nuclear magnetic resonance. J. Chem. Phys. 28, 430–431. doi:10.1063/1.1744152.

Meguro, R., Asano, A., Odagiri, S., Li, C., Shoumura, K., 2008. Cellular and subcellular localizations of nonheme ferric and ferrous iron in the rat brain: a light and electron microscopic study by the perfusion-Perls and -Turnbull methods. Arch. Histol. Cytol. 71, 205–222. doi:10.1679/aohc.71.205.

Mezer, A., Yeatman, J.D., Stikov, N., Kay, K.N., Cho, N.-J., Dougherty, R.F., Perry, M., Parvizi, J., Hua, L.H., Butts-Pauly, K., Wandell, B.A., 2013. Quantifying the local tissue volume and composition in individual brains with magnetic resonance imaging. Nat. Med. 19, 1667–1672. doi:10.1038/nm.3390.

Mispelter, J., Lupu, M., Briguet, A., 2006. NMR Probeheads for Biophysical and Biomedical Experiments. Theoretical Principles and Practical Guidelines. Imperial College Press, London, p. 280. doi:10.1142/P438.

Möller, H.E., Bossoni, L., Connor, J.R., Crichton, R.R., Does, M.D., Ward, R.J., Zecca, L., Zucca, F.A., Ronen, I., 2019. Iron, Myelin, and the brain: neuroimaging meets neurobiology. Trends Neurosci 42, 384–401. doi:10.1016/j.tins.2019.03.009.

Morris, C.M., Candy, J.M., Oakley, A.E., Bloxham, C.A., Edwardson, J.A., 1992. Histochemical distribution of non-haem iron in the human brain. Acta Anat 144, 235–257. doi:10.1159/000147312.

Morrison, C., Stanisz, G., Henkelman, R.M., 1995. Modeling magnetization transfer for biological-like systems using a semi-solid pool with a super-lorentzian lineshape and dipolar reservoir. J. Magn. Reson. B 108, 103–113. doi:10.1006/jmrb.1995.1111.

Müller, D.K., Pampel, A., Möller, H.E., 2013a. Matrix-algebra-based calculations of the time evolution of the binary spin-bath model for magnetization transfer. J. Magn. Reson. 230, 88–97. doi:10.1016/j.jmr.2013.01.013, Corrigendum. *J. Magn. Reson.* 2015; 261: 221://doi.org/10.1016/j.jmr.2015.11.001.

Müller, R., Pampel, A., Mildner, T., Marschner, H., Möller, H., 2013b. A transceive RF coil for imaging tissue specimen at 3T based on PCB design. In: Proceedings of the 21st Annual Meeting of ISMRM, Salt Lake City, UT, USA, p. 4366.

Newman, J.D., Kenkel, W.M., Aronoff, E.C., Bock, N.A., Zametkin, M.R., Silva, A.C., 2009. A combined histological and MRI brain atlas of the common marmoset monkey, *Callithrix jacchus*. Brain Res. Rev. 62, 1–18. doi:10.1016/j.brainresrev.2009.09.001.

Nieuwenhuys, R., 2012. The myeloarchitectonic studies on the human cerebral cortex of the Vogt-Vogt school, and their significance for the interpretation of functional neuroimaging data. Brain Struct. Funct. 218, 303–352. doi:10.1007/s00429-012-0460-z.

Norton, W.T., Cammer, W., 1984. Isolation and characterization of myelin. In: Morell, P. (Ed.), *Myelin.* Second Edition. Springer Science+Business Media, New York, NY, pp. 147–196.

Norton, W.T., Poduslo, S.R., 1973. Myelination in rat brain: changes in myelin composition during brain maturation. J. Neurochem. 21, 759–773. doi:10.1111/j.1471-4159.1973.tb07520.x.

O'Brian, J.S., Sampson, E.L., 1965. Lipid composition of the normal human brain: gray matter, white matter, and myelin. J. Lipid Res. 6, 537–544. doi:10.1016/S0022-2275(20)39619-X.

Palomero-Gallagher, N., Zilles, K., 2019. Cortical layers: cyto-, myelo, receptor- and synaptic architecture in human cortical areas. NeuroImage 197, 716–741. doi:10.1016/j.neuroimage.2017.08.035.

Pampel, A., Müller, D.K., Anwander, A., Marschner, H., Möller, H.E., 2015. Orientation dependence of magnetization transfer parameters in human white matter. NeuroImage 114, 136–146. doi:10.1016/j.neuroimage.2015.03.068.

Paxinos, G., Watson, C., Petrides, M., Rosa, M., Hironobu, T., 2012. The Marmoset Brain in Stereotaxic Coordinates. Academic Press, London, p. 282.

Pistorio, A.L., Hendry, S.H., Wang, X., 2006. A modified technique for high-resolution staining of myelin. J. Neurosci. Methods 153, 135–146. doi:10.1016/j.jneumeth.2005.10.014.

Portnoy, S., Stanisz, G.J., 2007. Modeling pulsed magnetization transfer. Magn. Reson. Med. 58, 144–155. doi:10.1002/mrm.21244.

Prevost, V.H., Yung, A., Morris, S.R., Vavasour, I.M., Samadi-Bahrami, Z., Moore, G.R.W., Laule, C., Mackay, A., Kozlowski, P., 2021. Temperature dependence and histological correlation of inhomogeneous magnetization transfer and myelin water imaging in ex vivo brain. NeuroImage 236, 118046. doi:10.1016/j.neuroimage.2021.118046.

Reinert, A., Morawski, M., Seeger, J., Arendt, T., Reinert, T., 2019. Iron concentrations in neurons and glial cells with estimates on ferritin concentrations. BMC Neurosci 20, 25. doi:10.1186/s12868-019-0507-7.

Rooney, W.D., Johnson, G., Li, X., Cohen, E.R., Kim, S.-G., Ugurbil, K., Springer Jr., C.S., 2007. Magnetic field and tissue dependencies of human brain longitudinal ^1H_2Orelaxation in Vivo. Magn. Reson. Med. 57,308–318. doi:10.1002/mrm.21122.

Salustri, C., 1996. Lack of magnetization transfer from the ferritin molecule. J. Magn. Reson. B 111, 171–173. doi:10.1006/jmrb.1996.0076.

Schmierer, K., Tozer, D.J., Scaravilli, F., Altmann, D.R., Barker, G.J., Tofts, P.S., Miller, D.H., 2007. Quantitative magnetization transfer imaging in postmortem multiple sclerosis brain. J. Magn. Reson. Imaging 26, 41–51. doi:10.1002/jmri.20984.

Schmierer, K., Wheeler-Kingshott, C.A.M., Tozer, D.J., Boulby, P.A., Parkes, H.G., Yousry, T.A., Scaravilli, F., Barker, G.J., Tofts, P.S., Miller, D.H., 2008. Quantitative magnetic resonance of postmortem multiple sclerosis brain before and after fixation. Magn. Reson. Med. 59, 268–277. doi:10.1002/mrm.21487.

Seifert, A.C., Umphlett, M., Hefti, M., Fowkes, M., Xu, J., 2019. Formalin tissue fixation biases myelin-sensitive MRI. Magn. Reson. Med. 82, 1504–1517. doi:10.1002/mrm.27821.

Sled, J.G., 2018. Modelling and interpretation of magnetization transfer imaging in the brain. NeuroImage 182, 128–135. doi:10.1016/j.neuroimage.2017.11.065.

Sled, J.G., Levesque, I., Santos, A.C., Francis, S.J., Narayanan, S., Brass, S.D., Arnold, D.L., Pike, G.B., 2004. Regional variations in normal brain shown by quantitative magnetization transfer imaging. Magn. Reson. Med. 51, 299–303. doi:10.1002/mrm.10701.

Sled, J.G., Pike, G.B., 2001. Quantitative imaging of magnetization transfer exchange and relaxation properties *in vivo* using MRI. Magn. Reson. Med. 46, 923–931. doi:10.1002/mrm.1278.

Smith, S.A., Bulte, J.W.M., van Zijl, P.C.M., 2009. Direct saturation MRI: theory and application to imaging brain iron. Magn. Reson. Med. 62, 384–393. doi:10.1002/mrm.21980.

Stanisz, G.J., Kecojevic, A., Bronskill, M.J., Henkelman, R.M., 1999. Characterizing white matter with magnetization transfer and T2. Magn. Reson. Med. 42, 1128–1136. doi:10.1002/(sici)1522-2594(199912)42:6<1128::aid–mrm18>3.0.co;2-9.

Stikov, N., Campbell, J.S.W., Stroh, T., Lavelée, M., Frey, S., Novek, J., Nuara, S., Ho, M.-K., Bedell, B.J., Dougherty, R.F., Leppert, I.R., Boudreau, M., Narayanan, S., Duval, T., Cohen-Adad, J., Picard, P.-A., Gasecka, A., Côté, D., Pike, G.B., 2015. *In vivo* histology of the myelin g-ratio with magnetic resonance imaging. NeuroImage 118, 397–405. doi:10.1016/j.neuroimage.2015.05.023.

Stüber, C., Morawski, M., Schäfer, A., Labadie, C., Wähnert, M., Leuze, C., Streicher, M., Barapatre, N., Reimann, K., Geyer, S., Spemann, D., Turner, R., 2014. Myelin and iron concentration in the human brain: a quantitative study of MRI contrast. NeuroImage 93, 95–106. doi:10.1016/j.neuroimage.2014.02.026.

Tomassy, G.S., Berger, D.R., Chen, H.-H., Kasthuri, N., Hayworth, K.J., Vercelly, A., Seung, H.S., Lichtman, J.W., Arlotta, P., 2014. Distinct profiles of myelin distribution along single axons of pyramidal neurons in the neocortex. Science 344, 319–324. doi:10.1126/science.1249766.

Trujillo, P., Summers, P.E., Ferrari, E., Zucca, F.A., Sturini, M., Mainardi, L.T., Cerutti, S., Smith, A.K., Smith, S.A., Zecca, L., Costa, A., 2017a. Contrast mechanisms associated with neuromelanin-MRI. Magn. Reson. Med. 78, 1790–1800. doi:10.1002/mrm.26584.

Trujillo, P., Summers, P.E., Smith, A.K., Smith, S.A., Mainardi, L.T., Cerutti, S., Claassen, D.O., Costa, A., 2017b. Pool size ratio of the substantia nigra in Parkinson's disease derived from two different quantitative magnetization transfer approaches. Neuroradiology 59, 1251–1263. doi:10.1007/s00234-017-1911-2.

Tyler, D.J., Gowland, P.A., 2005. Rapid quantitation of magnetization transfer using pulsed off-resonance irradiation and echo planar imaging. Magn. Reson. Med. 53, 103–109. doi:10.1002/mrm.20323.

Uchihara, T., 2007. Silver diagnosis in neuropathology: principles, practice and revised interpretation. Acta Neuropathol 113, 483–499. doi:10.1007/s00401-007-0200-2.

Vavasour, I.M., Whittall, K.P., MacKay, A.L., Li, D.K.B, Vorobeychik, G., Paty, D.W., 1998. A comparison between magnetization transfer ratios and myelin water percentages in normals and multiple sclerosis patients. Magn. Reson. Med. 40, 763–768. doi:10.1002/mrm.1910400518.

Wang, Y.C., van Gelderen, P., de Zwart, J.A., Duyn, J.H., 2020. B0-field dependence of MRI T1 relaxation in human brain. NeuroImage 213, 116700. doi:10.1016/j.neuroimage.2020.116700.

Watanabe, O., West, C.R., Bremer, A., 1977. Experimental regional cerebral ischemia in the middle cerebral artery territory in primates. Part 2: effects on brain water and electrolytes in the early phase of MCA stroke. Stroke 8, 71–76. doi:10.1161/01.str.8.1.71.

Weiss, M., Alkemade, A., Keuken, M.C., Müller-Axt, C., Geyer, S., Turner, R., Forstmann, B.U., 2015. Spatial normalization of ultrahigh resolution 7 T magnetic resonance imaging data of the postmortem human subthalamic nucleus: a multistage approach. Brain Struct. Funct. 220, 1695–1703. doi:10.1007/s00429-014-0754-4.

Wennerström, H., 1973. Proton nuclear magnetic resonance lineshapes in lamellar liquid crystals. Chem. Phys. Lett. 18, 41–44. doi:10.1016/0009-2614(73)80333-1.

Wolff, S.D., Balaban, R.S., 1989. Magnetization transfer contrast (MTC) and tissue water proton relaxation *in vivo*. Magn. Reson. Med. 10, 135–144. doi:10.1002/mrm.1910100113.

Yuasa, S., Nakamura, K., Kohsaka, S., 2010. Stereotaxic Atlas of the Marmoset Brain. With Immunohistochemical Architecture and MR Images. National Institute of Neuroscience, Tokyo.